

## THE X-RAY LUMINOSITY FUNCTIONS OF FIELD LOW-MASS X-RAY BINARIES IN EARLY-TYPE GALAXIES: EVIDENCE FOR A STELLAR AGE DEPENDENCE

B. D. LEHMER<sup>1,2</sup>, M. BERKELEY<sup>2,3</sup>, A. ZEAS<sup>4,5,6</sup>, D. M. ALEXANDER<sup>7</sup>, A. BASU-ZYCH<sup>2,8</sup>, F. E. BAUER<sup>9,10</sup>, W. N. BRANDT<sup>11,12</sup>,  
 T. FRAGOS<sup>5</sup>, A. E. HORNSCHMEIER<sup>2</sup>, V. KALOGERA<sup>13</sup>, A. PTAK<sup>2</sup>, G. R. SIVAKOFF<sup>14</sup>, P. TZANAVARIS<sup>1,2</sup>, AND M. YUKITA<sup>1,2</sup>

<sup>1</sup> The Johns Hopkins University, Homewood Campus, Baltimore, MD 21218, USA

<sup>2</sup> NASA Goddard Space Flight Center, Code 662, Greenbelt, MD 20771, USA

<sup>3</sup> Institute for Astrophysics and Computational Sciences, Department of Physics, The Catholic University of America, Washington, DC 20064, USA

<sup>4</sup> Physics Department, University of Crete, Heraklion, Greece

<sup>5</sup> IESL, Foundation for Research and Technology, 71110 Heraklion, Crete, Greece

<sup>6</sup> Harvard-Smithsonian Center for Astrophysics, 60 Garden Street, Cambridge, MA 02138, USA

<sup>7</sup> Department of Physics, University of Durham, South Road, Durham DH1 3LE, UK

<sup>8</sup> Center for Space Science and Technology, University of Maryland Baltimore County, 1000 Hilltop Circle, Baltimore, MD 21250, USA

<sup>9</sup> Pontificia Universidad Catolica de Chile, Departamento de Astronomia y Astrofisica, Casilla 306, Santiago 22, Chile

<sup>10</sup> Space Science Institute, 4750 Walnut Street, Suite 205, Boulder, CO 80301, USA

<sup>11</sup> Department of Astronomy and Astrophysics, Pennsylvania State University, University Park, PA 16802, USA

<sup>12</sup> Institute for Gravitation and the Cosmos, Pennsylvania State University, University Park, PA 16802, USA

<sup>13</sup> Department of Physics and Astronomy, Northwestern University, 2145 Sheridan Road, Evanston, IL 60208, USA

<sup>14</sup> Department of Physics, University of Alberta, CCIS 4-183 Edmonton, AB T6G 2E1, Canada

Received 2014 March 10; accepted 2014 May 8; published 2014 June 13

### ABSTRACT

We present direct constraints on how the formation of low-mass X-ray binary (LMXB) populations in galactic fields depends on stellar age. In this pilot study, we utilize *Chandra* and *Hubble Space Telescope* (*HST*) data to detect and characterize the X-ray point source populations of three nearby early-type galaxies: NGC 3115, 3379, and 3384. The luminosity-weighted stellar ages of our sample span  $\approx 3$ –10 Gyr. X-ray binary population synthesis models predict that the field LMXBs associated with younger stellar populations should be more numerous and luminous per unit stellar mass than older populations due to the evolution of LMXB donor star masses. Crucially, the combination of deep *Chandra* and *HST* observations allows us to test directly this prediction by identifying and removing counterparts to X-ray point sources that are unrelated to the field LMXB populations, including LMXBs that are formed dynamically in globular clusters, Galactic stars, and background active galactic nuclei/galaxies. We find that the “young” early-type galaxy NGC 3384 ( $\approx 2$ –5 Gyr) has an excess of luminous field LMXBs ( $L_X \gtrsim (5\text{--}10) \times 10^{37} \text{ erg s}^{-1}$ ) per unit *K*-band luminosity ( $L_K$ ; a proxy for stellar mass) than the “old” early-type galaxies NGC 3115 and 3379 ( $\approx 8$ –10 Gyr), which results in a factor of  $\approx 2$ –3 excess of  $L_X/L_K$  for NGC 3384. This result is consistent with the X-ray binary population synthesis model predictions; however, our small galaxy sample size does not allow us to draw definitive conclusions on the evolution field LMXBs in general. We discuss how future surveys of larger galaxy samples that combine deep *Chandra* and *HST* data could provide a powerful new benchmark for calibrating X-ray binary population synthesis models.

**Key words:** galaxies: elliptical and lenticular, cD – galaxies: evolution – Galaxy: stellar content – globular clusters: general – X-rays: binaries – X-rays: galaxies

*Online-only material:* color figures

### 1. INTRODUCTION

The *Chandra X-ray Observatory* (*Chandra*) has contributed greatly to our understanding of compact objects (e.g., neutron stars and black holes) through the study of X-ray binary populations in normal galaxies. Through correlative studies involving X-ray binary populations and galaxy physical properties (e.g., stellar mass and stellar ages), we have gained insight into the key factors that influence the formation and evolution of compact objects, the stars involved in the accreting binary phase, and their associated remnants (e.g., millisecond pulsars and compact-object binaries). However, a comprehensive understanding of the formation and evolution of compact objects will require empirical constraints on X-ray binary populations in galaxies at a variety of evolutionary stages.

In the Milky Way, it has been observed that low-mass X-ray binaries (LMXBs) are the dominant luminous accreting binary population, and are collectively a factor of  $\approx 10$  times more luminous than the high-mass X-ray binaries (e.g., Grimm et al. 2002). With the advent of sub-arcsecond imaging with *Chandra*, it has now been shown that LMXB populations are

prevalent in other nearby galaxies (e.g., Fabbiano 2006, and references therein). *Chandra* studies of X-ray binaries in local galaxies have found that the galaxy-wide integrated X-ray power from LMXBs is strongly correlated with galaxy stellar mass ( $M_*$ ; e.g., O’Sullivan et al. 2001; Colbert et al. 2004; Gilfanov 2004; Kim & Fabbiano 2010; Lehmer et al. 2010; Boroson et al. 2011; Zhang et al. 2012). However, in early-type galaxies, the rms scatter in the  $L_X$ – $M_*$  relation is found to be  $\approx 40\%$ , which is a factor of  $\gtrsim 3$ –5 times larger than typical measurement error and a factor of  $\approx 2$  times larger than that expected from statistical variations due to small number statistics (see Gilfanov 2004). This indicates that additional factors (e.g., stellar age and globular cluster (GC) LMXB systems) aside from  $M_*$  alone influence the prevalence of LMXBs in galaxies.

Population synthesis models predict that  $L_X$  per  $M_*$  for LMXBs in galactic fields should decrease with increasing stellar age. This is primarily due to a decline in the typical masses of LMXB donor stars, and X-ray luminosities, with increasing stellar age (e.g., Belczynski et al. 2002, 2008; Fragos et al. 2008, 2013a, 2013b). Initial observational tests of these models have yielded conflicting results. In support of the population

synthesis predictions, Kim & Fabbiano (2010) studied samples of seven young ( $\approx 2\text{--}5$  Gyr) and seven old ( $\approx 8\text{--}12$  Gyr) nearby early-type galaxies using *Chandra* observations that probe the  $L_X \gtrsim 10^{38}$  erg s $^{-1}$  end of the X-ray binary luminosity function (XLF). Their observations showed that the fraction of LMXBs that were more luminous than  $\approx 5 \times 10^{38}$  erg s $^{-1}$  is a factor of  $\approx 2$  times higher ( $\approx 3\sigma$ ) for the young early-type galaxy sample. Further support for the population synthesis expectation came from Lehmer et al. (2007), who utilized X-ray stacking analyses in the Extended Chandra Deep Field-South survey to find that optically faint early-type galaxies ( $L_B \approx 10^{9.5}\text{--}10^{10} L_{B,\odot}$ ), a population expected to have X-ray emission dominated by LMXBs, have mean LMXB emission that is a factor of  $\approx 3\text{--}8$  times larger at  $z \approx 0.4$  ( $\approx 4$  Gyr ago) than today. More recently, however, Zhang et al. (2012) constructed detailed LMXB XLFs for a sample of 20 early-type galaxies spanning luminosity-weighted stellar ages of 1.6–17 Gyr and found an *increase* in the *K*-band luminosity normalized LMXB XLF normalization with increasing stellar age. The same conclusion can be drawn from the total LMXB  $L_X/L_K$  versus stellar age diagrams constructed from the sample of 30 early-type galaxies studied by Boroson et al. (2011; see Section 6 and Figure 9(a)). These studies seemingly contradict previous results and the population synthesis expectation.

Although the above studies and theoretical expectations seem to show apparent conflict, many of the differences between studies can be explained by inhomogeneities in the galaxy samples and LMXB populations being studied. Although there has been substantial efforts on dynamic modeling of GCs, published population synthesis modeling exclusively follows the evolution of LMXBs produced in primordial binaries formed in galactic fields (hereafter, field LMXBs) and does not make simultaneous predictions for LMXBs formed in GCs. The GC LMXBs form efficiently through dynamical interactions of multiple bodies (e.g., Fabian et al. 1975; Hills 1976; Verbunt 1987), and their formation is expected to be tied to the dynamical and chemical properties of the host GC with little relation to the host galaxy stellar population age. In GCs, LMXBs are expected to form continuously as stars interact dynamically. While in galactic fields, LMXB formation and emission is expected to be directly connected to stellar evolution timescales of the secondary stars, lagging Gyrs behind previous star-formation episodes.

Detailed studies of LMXB populations of local early-type galaxies have been substantially biased toward massive galaxies, which tend to have rich GC systems (e.g., Bekki et al. 2006) and LMXB populations dominated by GC LMXBs and not field LMXBs (e.g., Irwin 2005). Going forward, it will be critical to test population synthesis models by studying specifically the *field LMXB* populations in a sample of passive galaxies with stellar populations that cover a large range of stellar ages. The combination of deep *Chandra* and *Hubble Space Telescope* (*HST*) imaging offers a means for identifying and separating LMXBs that are formed in galactic fields and GCs (e.g., Voss et al. 2009). At present, such a study has yet to be performed, primarily because the necessary deep *Chandra* and *HST* observations of early-type galaxies with relatively young to intermediate stellar ages ( $\approx 3\text{--}5$  Gyr) had not yet been undertaken.

To remedy the above limitation, we have conducted a pilot program consisting of deep *Chandra* and *HST* observations of the nearby early-type galaxy NGC 3384, which has a luminosity-weighted stellar age of  $\approx 3.2 \pm 1.5$  Gyr (e.g.,

McDermid et al. 2006; Sánchez-Blázquez et al. 2007). In this paper, we utilize our new *Chandra* and *HST* data to construct the field LMXB XLF for the “young” stellar population in NGC 3384. We compare the field LMXB XLF of NGC 3384 with those derived using deep archival *Chandra* and *HST* data of two “old” early-type galaxies, NGC 3115 and NGC 3379, which have luminosity-weighted stellar ages of  $8.5 \pm 1.0$  and  $8.6 \pm 1.0$  Gyr (Sánchez-Blázquez et al. 2006), respectively. The stellar ages for the whole sample are based on results from simple stellar population model fitting to both absorption lines and spectral energy distribution shapes. In this process, absorption-line strengths were all calibrated to the Lick/IDS system (e.g., Trager et al. 1998) and stellar ages were determined by interpolating between multidimensional model grids of absorption line indices and ages. All three galaxies have been shown to have smooth spatial distributions of luminosity-weighted stellar ages consistent with no significant age variations across the galactic extents (Norris et al. 2006; Sánchez-Blázquez et al. 2007).

Throughout this paper, we make use of three X-ray band-passes: 0.5–2 keV (soft band (SB)), 2–8 keV (hard band (HB)), and 0.5–8 keV (full band (FB)). Values of  $H_0 = 70$  km s $^{-1}$  Mpc $^{-1}$ ,  $\Omega_M = 0.3$ , and  $\Omega_\Lambda = 0.7$  are adopted throughout this paper (e.g., Spergel et al. 2003).

## 2. EARLY-TYPE GALAXY SAMPLE SELECTION

Our primary goal is to measure and compare field LMXB XLFs down to a relatively faint X-ray luminosity limit for early-type galaxies spanning a wide range of stellar ages. We therefore required a sample of early-type galaxies with deep *Chandra* observations that have corresponding *HST* imaging across the whole galactic extents.

Using a base sample of 376 nearby early-type galaxies from Ellis & O’Sullivan (2006), we searched the *Chandra* archive (from Cycle 12) for observations that were sufficient to detect X-ray point sources to a highly complete 0.5–8 keV depth of  $L_X \approx 10^{37}$  erg s $^{-1}$ , an important limit above which a significant number of LMXBs can be detected (see below) and a variety of LMXB donors and accretors are expected to contribute (Fragos et al. 2008). The Ellis & O’Sullivan (2006) sample was selected from the Lyon–Meudon Extragalactic Data Archive using morphological type ( $T < 1.5$ ; E–S0 Hubble types), distance ( $V \leq 9000$  km s $^{-1}$ ), and apparent magnitude ( $B_T \leq 13.5$ ). To probe effectively the stellar-age dependent LMXB activity in early-type galaxies, we isolated galaxies that (1) contain passive stellar populations with little ongoing star-formation as measured by detailed *Spitzer* studies (e.g., Temi et al. 2009; Shapiro et al. 2010); (2) have small values of GC specific frequency,  $S_N \lesssim 3$ , (where  $S_N \equiv N_{GC} 10^{0.4(M_V+15)}$ ,  $N_{GC}$  is the number of GCs within the galaxy, and  $M_V$  is the absolute *V*-band magnitude of the galaxy), to study optimally both field and GC LMXBs, but without GC LMXBs dominating (e.g., Kim & Fabbiano 2004; Irwin 2005; Juett 2005; Boroson et al. 2011; Zhang et al. 2012); (3) have distances  $D \lesssim 15$  Mpc, so as to avoid serious confusion issues, and (4) have *K*-band luminosities (a proxy for stellar mass) in a relatively small range  $L_K \approx 2\text{--}10 \times 10^{10} L_{K,\odot}$ .<sup>15</sup> The final *K*-band luminosity criterion removes large variations in LMXB populations that might arise as a result of the  $L_X\text{--}M_\star$  relation, ensures that a sufficient, statistically meaningful number of LMXBs ( $\gtrsim 50\text{--}100$ ) per

<sup>15</sup> *K*-band luminosities were computed using data from the Two Micron All Sky Survey (2MASS) large galaxy atlas (Jarrett et al. 2003) and *K*-band extended source catalogs. The 2MASS extended source catalog is available online via <http://tdc-www.harvard.edu/catalogs/tmxsc.html>.

**Table 1**  
Properties of Early-type Galaxy Sample

Galaxy (1)	K-band Position		$D$ (Mpc)	$a$ (arcmin)	$b$ (arcmin)	P.A. (deg)	$r_{\text{exclude}}$ (arcsec)	$\log L'_K$ ( $L_{K,\odot}$ )	$f_{K,\text{exclude}}$	$S_N$ (11)	Age (Gyr)	SFR ( $M_\odot \text{ yr}^{-1}$ )
	$\alpha_{J2000}$ (hr)	$\delta_{J2000}$ (deg)										
NGC 3115	10 05 14.0	−07 43 07	$9.68 \pm 0.41$	2.7	1.1	315	20	$10.95 \pm 0.04$	0.46	$2.3 \pm 0.5$	$8.5^{+1.0}_{-1.0}$ <sup>a</sup>	<0.004
NGC 3379	10 47 49.6	+12 34 53	$10.57 \pm 0.55$	3.2	2.7	338	10	$10.89 \pm 0.05$	0.25	$1.3 \pm 0.7$	$8.6^{+1.0}_{-1.0}$ <sup>a</sup>	<0.004
NGC 3384	10 48 16.9	+12 37 45	$11.59 \pm 0.77$	3.5	1.8	321	20	$10.78 \pm 0.06$	0.47	$1.1 \pm 0.5$	$3.2^{+1.5}_{-1.0}$ <sup>b</sup>	<0.009

**Notes.** Column 1: target name. Columns 2 and 3: right ascension and declination, respectively, based on  $K$ -band data from the 2MASS large galaxy atlas (Jarrett et al. 2003). Column 4: distance and  $1\sigma$  error as determined by Tonry et al. (2001). Columns 5–7:  $K$ -band galaxy major axis, minor axis, and position angle, respectively. Column 8: radius of a small circular region, centered on the galactic nucleus, that was excluded from further analyses due to both the presence of a bright optical background from the galactic stellar field and significant X-ray source confusion. Column 9: logarithm of the total galaxy-wide  $K$ -band luminosity and  $1\sigma$  error. The  $1\sigma$  errors are dominated by the errors on the distances (see Column 4). These luminosities have *not* been corrected for the excluded region specified in Column 8. Column 10: fraction of the total galaxy-wide  $K$ -band luminosity contained within the excluded region. The final  $L_K$  value used in most calculations throughout this paper can be calculated as  $L_K = L'_K \times (1 - f_{K,\text{exclude}})$ , where  $L'_K$  is the value provided in Column 9. For our sample,  $L_K$  and  $L'_K$  can be converted to stellar mass using  $M_*/L_K \approx 0.66 M_\odot/L_{K,\odot}$ , appropriate for all three galaxies. Column 11: globular cluster specific frequency  $S_N$  from Harris (1991). Column 12: stellar age estimates. Column 13: integrated galaxy-wide star-formation rates inferred from *Spitzer* from Temi et al. (2009) or Shapiro et al. (2010). <sup>a</sup>Sánchez-Blázquez et al. (2006). <sup>b</sup>McDermid et al. (2006).

galaxy are detected above  $L_X \approx 10^{37} \text{ erg s}^{-1}$ , and minimizes contributions from hot X-ray gas that are prevalent in more massive early-type galaxies (David et al. 2006).

From the criteria above, we found that three galaxies, Cen A, NGC 3115, and NGC 3379 had sufficient *Chandra* coverage to study in detail LMXB XLFs; however, Cen A is problematic for our program since it has highly uncertain global stellar population ages due to large dust lanes, shows signatures of recent gas-rich merger activity (e.g., Kainulainen et al. 2009), and further contains bright extended X-ray structures (shells and a jet) making it difficult to study the XRB populations (e.g., Voss et al. 2009). By contrast, NGC 3115 and 3379 have deep *Chandra* and *HST* exposures and satisfy all four selection criteria posed above; therefore, they are ideal candidates to include in our program (see, e.g., Kim et al. 2006, 2009; Brasington et al. 2008, 2010). These galaxies have been determined to have relatively old stellar populations ( $\approx 8$ – $10$  Gyr based on multiple stellar age measurements) and therefore these *Chandra* and *HST* observations have the potential to provide key observational constraints for “old” field LMXB populations.

Using the remaining early-type galaxy sample that did not have deep *Chandra* data in the archive, we searched for “young” ( $\lesssim 5$  Gyr) early-type galaxy candidates to target with *Chandra* and *HST*. We found that NGC 3377 and 3384 were the nearest sources ( $D < 15$  Mpc) that have relatively young stellar populations and satisfy our selection criteria. In Cycle 13, we successfully proposed for joint *Chandra* and *HST* observations of NGC 3384, which we present for the first time in this paper. Taken together, NGC 3115, 3379, and 3384 form a clean sample of passive  $D < 15$  Mpc early-type galaxies with stellar ages ranging from  $\approx 3$ – $10$  Gyr. The *Chandra* and *HST* observations of all three galaxies cover the entire  $K$ -band extents and reach  $0.5$ – $8$  keV limits of  $\lesssim 10^{37} \text{ erg s}^{-1}$ . The  $K$ -band luminosities provide good proxies for the stellar masses  $M_*$  of the galaxies in our study. Adopting the prescription outlined in Appendix 2 of Bell et al. (2003), we utilized  $B - V$  colors to estimate that  $M_*/L_K \approx 0.66 M_\odot/L_{K,\odot}$  for all three galaxies in our sample. We note that this method has an uncertainty of  $\approx 0.1$ – $0.2$  dex on the derived  $M_*/L_K$  for a given  $B - V$  color. It is likely the case that the younger galaxy NGC 3384 has a *true*  $M_*/L_K$  that is lower than those for the two older galaxies NGC 3115 and 3379. Hereafter, we make use of scalings with  $L_K$ , and where appropriate, convert to  $M_*$  using a constant  $M_*/L_K$  conversion

factor for the whole sample. In Table 1, we summarize the properties of the galaxies that make up our sample and in Section 3 we describe our *Chandra* and *HST* data and analyses.

### 3. DATA REDUCTION

As discussed in Section 2, we are comparing results from new *Chandra* and *HST* observations of the “young” early-type galaxy NGC 3384 with comparable-to-better quality archival data for “old” early-type galaxies NGC 3115 and NGC 3379. We note that there are published papers describing some of the *Chandra* and *HST* archival data available for NGC 3115 and NGC 3379 (e.g., Brasington et al. 2008, 2010, 2012; Wong et al. 2013); however, to limit comparison errors, we analyze the *Chandra* and *HST* data for all three galaxies using the methodologies adopted in this paper. In the sections below, we describe our data reduction methods in detail.

#### 3.1. Chandra Data Reduction and X-Ray Catalog Creation

The *Chandra* observations for all three galaxies were conducted in multiple observations (hereafter, Obs. IDs) using the S-array of the Advanced CCD Imaging Spectrometer (ACIS-S; see Table 2 for full observation log). The  $K$ -band semi-major axes of the galaxies (Column 5 of Table 1) range from  $2.7$  to  $3.5$  and therefore subtend an angular extent smaller than a single ACIS-S chip ( $\approx 8.5 \times 8.5$ ). As such, for all *Chandra* observations, the galactic extents were almost entirely contained within the ACIS-S3 chip for all observations. For our data reduction, we made use of CIAO version 4.5 with CALDB version 4.5.6. We began by reprocessing the pipeline produced events lists, bringing level 1 to level 2 using the script `chandra_repro`. The `chandra_repro` script runs a variety of CIAO tools that identify and remove events from bad pixels and columns, and filter the events list to include only good time intervals without significant flares and non-cosmic ray events corresponding to the standard ASCA grade set (ASCA grades 0, 2, 3, 4, 6).

Using the reprocessed level 2 events lists for each Obs. ID, we generated preliminary FB images and point-spread function (PSF) maps (using the tool `mkpsfmap`) with a monochromatic energy of  $1.497$  keV and an encircled counts fraction set to  $0.393$ . For each Obs. ID, we created preliminary source catalogs by searching the FB images with `wavdetect` (run including our PSF map), which was set at a false-positive probability threshold of  $1 \times 10^{-5}$  and run over seven wavelet scales from  $1$  to  $8$  pixels ( $1, \sqrt{2}, 2, 2\sqrt{2}, 4, 4\sqrt{2}$ , and  $8$ ). To measure sensitively

**Table 2**  
*Chandra* Advanced CCD Imaging Spectrometer (ACS) Observation Log

Galaxy	Obs. ID	Obs. Start (UT)	Exposure Time <sup>a</sup> (ks)	Flaring <sup>b</sup> Intervals	Flaring Time <sup>b</sup> (ks)	Obs. Mode <sup>c</sup>
NGC 3115	2040	2001 Jun 14, 10:31	35.3	1	1.6	F
	11268	2010 Jan 27, 00:42	40.6	0	...	VF
	12095	2010 Jan 29, 14:29	75.7	0	...	VF
	13817	2012 Jan 18, 14:08	172.0	0	...	VF
	13819	2012 Jan 26, 22:21	70.0	2	5.5	VF
	13820 <sup>d</sup>	2012 Jan 31, 14:55	184.2	0	...	VF
	13821	2012 Feb 3, 09:39	157.5	1	0.5	VF
	13822	2012 Jan 21, 08:54	143.0	2	17.2	VF
	14383	2012 Apr 4, 02:37	119.0	1	0.5	VF
	14384	2012 Apr 6, 17:51	69.7	0	...	VF
	14419	2012 Apr 5, 18:49	46.3	0	...	VF
	Merged	...	<b>1113.3</b>	7	25.3	...
	1587	2001 Feb 13, 01:33	30.5	2	1.0	F
	7073 <sup>d</sup>	2006 Jan 1, 05:50	81.6	3	2.5	F
NGC 3379	7074	2006 Apr 9, 10:34	69.1	0	...	VF
	7075	2006 Jul 3, 11:04	82.1	2	1.0	VF
	7076	2007 Jan 10, 01:51	69.2	0	...	VF
	Merged	...	<b>333.5</b>	7	4.5	...
	4692	2004 Oct 19, 18:57	9.9	0	...	VF
NGC 3384	11782	2010 Jan 19, 11:31	28.2	1	0.5	F
	13829 <sup>d</sup>	2012 Jun 23, 11:07	94.8	0	...	VF
	Merged	...	<b>132.9</b>	1	0.5	...

**Notes.** Links to the data sets in this table have been provided in the electronic edition. Values in bold are the merged exposure times and represent the total depth of the resulting *Chandra* data set used in the analyses.

<sup>a</sup> All observations were continuous. These times have been corrected for removed data that was affected by high background; see Section 3.1.

<sup>b</sup> Number of flaring intervals and their combined duration. These intervals were rejected from further analyses.

<sup>c</sup> The observing mode (F = Faint mode; VF = Very Faint mode).

<sup>d</sup> Indicates Obs. ID by which all other observations are reprojected to for alignment purposes. This Obs. ID was chosen for reprojection as it had the longest initial exposure time, before flaring intervals were removed.

whether any significant flares remained in our observations, we constructed point-source-excluded 0.5–8 keV background light curves for each Obs. ID with 500 s time bins. For each galaxy, we found 1–7 intervals across all Obs. IDs with flaring events of  $\gtrsim 3\sigma$  above the nominal background; these intervals were removed from further analyses (see Table 2). In general, this resulted in the removal of short intervals; however, for NGC 3115  $\approx 25$  ks of data were excluded. The resulting cumulative exposure times for NGC 3115, 3379, and 3384 were 1,113 ks, 333 ks, and 133 ks, respectively.

For each galaxy and Obs. ID, we utilized the preliminary source catalogs based on *wavdetect* positions to register each good-time-interval screened aspect solution and events list to the frame with the longest exposure time (see Table 2); this was achieved using CIAO tools *reproject\_aspect* and *reproject\_events*, respectively. The resulting astrometric reprojections gave nearly negligible linear translations ( $< 0.38$  pixels), rotations ( $< 0.1$  deg), and stretches ( $< 0.06\%$  of the pixel size) for all Obs. IDs. We created merged events lists for each galaxy using the reprojected events lists and the CIAO script *merge\_obs*. In Figure 1, we show adaptively smoothed, false-color images for the three merged data sets.

Using the individual Obs. ID and merged events lists, we constructed images for each galaxy in the FB, SB, and HB. For each of the three bands, we created corresponding exposure maps following the basic procedure outlined in Section 3.2 of Hornschemeier et al. (2001); these maps were normalized to the effective exposures of sources located at the aim points. This procedure takes into account the effects of vignetting,

gaps between the CCDs, bad column and pixel filtering, and the spatially dependent degradation of the ACIS optical blocking filter. A photon index of  $\Gamma = 1.4$ , the slope of the extragalactic cosmic X-ray background in the FB (e.g., Hickox & Markevitch 2006), was assumed in creating the exposure maps.

For a given galaxy, we created a *candidate source catalog* by first searching each image (i.e., all Obs. IDs and merged images in all three bands) using *wavdetect* at a liberal false-positive probability threshold of  $1 \times 10^{-5}$  over the  $\sqrt{2}$  sequence (see above). We searched all Obs. IDs to isolate the locations of transient source candidates that may have been diluted by background and thus not detected by *wavdetect* in the merged image. We then merged the *wavdetect* catalogs together by cross-matching the point-source catalogs. For a given galaxy, we cross-matched the catalogs using matching radii of  $1''.5$ ,  $2''.5$ , and  $3''.5$  for sources offset by  $\lesssim 2'$ ,  $2'-6'$ , and  $\gtrsim 6'$ , respectively, from the exposure-weighted average aim-point location. We inspected all the images and candidate source regions by eye to see if any additional source candidates were missed. In particular, in the crowded nuclear regions of the elliptical galaxies, low-flux point sources may not be picked up by *wavdetect* due to the complex backgrounds. As a result of our inspection, we identified six additional candidate sources, including three, one, and two sources in the nuclear regions of NGC 3115, 3379, and 3384, respectively, which we added to our candidate source catalogs.

We performed detailed photometry on our candidate source catalogs using the ACIS *EXTRACT* (hereafter AE; Broos et al.

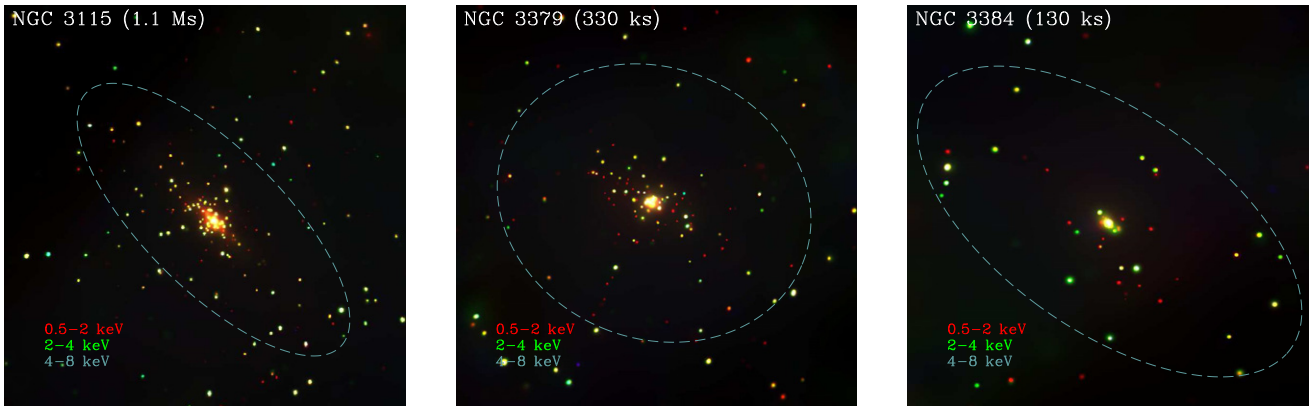


**Figure 1.** Three-color *Chandra* images of the three early-type galaxies in our sample. Each image was constructed from 0.5–2 keV (red), 2–4 keV (green), and 4–8 keV (blue) exposure-corrected adaptively smoothed images. Dashed ellipses represent the total *K*-band galaxy size and orientation as described in Columns 2, 3, and 5–7 of Table 1. We note that the range of the *Chandra* image depths (see annotations) is large (0.1–1.1 Ms), thus affecting comparative quality.

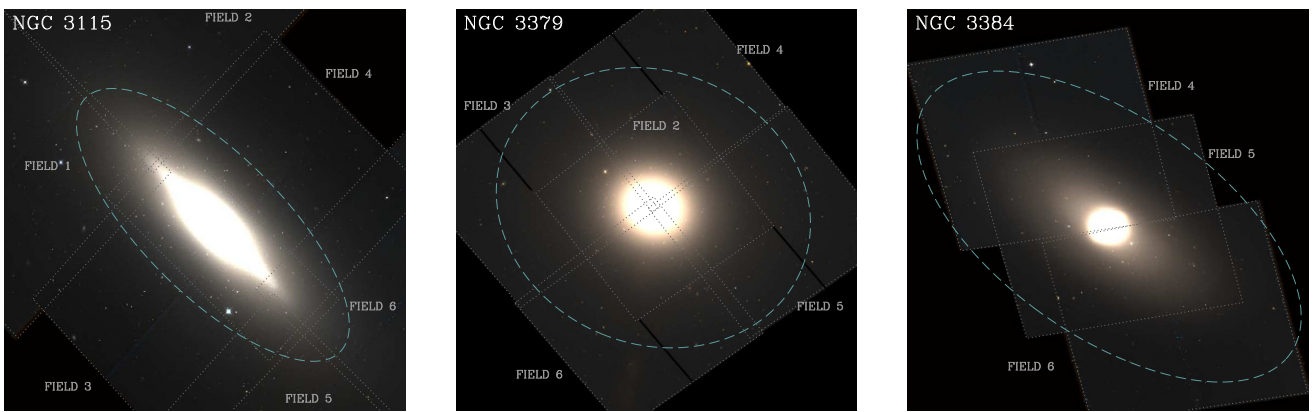


**Figure 2.** Color *HST* ACS mosaics of the three early-type galaxies in our sample. Each image was constructed using F850LP (red), (F850LP + F475W)/2 (green), and F475W (blue) image mosaics. Image sizes, orientations, and dashed ellipses are the same as in Figure 1. Each  $202'' \times 202''$  ACS field of view has been outlined (solid squares) and the field name annotated. A description of our mosaicking procedure can be found in Section 3.2.

2010) point-source analysis software and the *wavdetect*-based positions.<sup>16</sup> The AE software contains algorithms that allow for appropriate computation of source properties when multiple observations with different roll angles and/or aim points are being combined and analyzed (see discussion below for further details). AE also uses complex algorithms for accurately computing the photometry of sources in crowded regions like those found in the nuclear regions of our early-type galaxies. The improved photometry provided by AE allows us to evaluate clearly the significances of the point sources in each candidate source catalog and prune our source lists to include reliable sources. For a source to be considered detected, it must contain  $s$  counts within an aperture representing  $\approx 90\%$  of the point-source encircled-energy fraction (EEF) satisfying the following binomial probability criterion:

$$P(x \geq s) = \sum_{x=s}^n \frac{n!}{x!(n-x)!} p^x (1-p)^{n-x} \leq P_{\text{thresh}}, \quad (1)$$

where  $n \equiv s + b_{\text{ext}}$  and  $p \equiv 1/(1 + b_{\text{ext}}/b_{\text{src}})$ . Here  $b_{\text{ext}}$  is the total number of background counts extracted from a large region outside of the point source (while masking out regions from other X-ray-detected sources) that was used to obtain an estimate of the local background count rate. The quantity  $b_{\text{src}}$  is

the estimated number of background counts within the source extraction region, which was measured by rescaling  $b_{\text{ext}}$  to the area of the source aperture (the inter-quartile range of  $b_{\text{ext}}/b_{\text{src}} \approx 24\text{--}118$ ). We adopted a threshold value of  $P_{\text{thresh}} = 0.004$ , below which we considered a source candidate to be a valid X-ray point source and unlikely to be a fluctuation of the background. Our choice was motivated by the Xue et al. (2011) analysis of the 4 Ms *Chandra* Deep Field-South survey, in which the use of  $P_{\text{thresh}} = 0.004$  maximized the number of valid sources that had optical/near-IR counterparts without introducing a significant number of false sources.

For each galaxy, we constructed *main catalogs* by iteratively pruning our candidate source lists to include only sources with  $P \leq P_{\text{thresh}}$  in at least one of the three bandpasses. In this process, we first computed  $P$  using *only* the merged photometry,<sup>17</sup> we then re-extracted source and background counts from the remaining sources, and repeated the process until no further sources were removed. The three galaxies required one to three iterations before converging.

We note that our multi-stage procedure for identifying a highly reliable list of source candidates will not result in a com-

<sup>16</sup> The ACIS EXTRACT software is available online at [http://www.astro.psu.edu/xray/docs/TARA/ae\\_users\\_guide.html](http://www.astro.psu.edu/xray/docs/TARA/ae_users_guide.html).

<sup>17</sup> Had we chosen to consider  $P$  computed from both the merged observations and each of the individual observations, additional faint variable sources would be included in our main catalogs. However, the deliberate inclusion of such sources would result in biasing our XLFs upward for increasing numbers of Obs. IDs. To some extent, bright variable sources may have a small effect on our results, if the sources are detected in the merged images.

plete selection of all real sources in each image having binomial probabilities  $\leq P_{\text{thresh}}$ , since the initial wavdetect selection has more complex source-detection criteria (see Freeman et al. 2002 for details) than the simple criterion given in Equation (1). Such a caveat is important when considering completeness of our X-ray catalogs. In Section 5 we discuss our methods for correcting for these completeness issues when computing LMXB XLFs.

### 3.2. HST Data Reduction and Optical Catalog Creation

Each of the three galaxies was observed with *HST* using the Advanced Camera for Surveys (ACS) with the F475W and F850LP filters, hereafter the  $g_{475}$  and  $z_{850}$  bands, respectively. The ACS field of view subtends an area of  $\approx 202'' \times 202''$ ; therefore the full mapping of each galaxy required multiple pointings. For a given galaxy, each ACS pointing pattern was carefully chosen to cover the entire optical extent of the galaxy and achieve higher sensitivity near the galactic center. High sensitivity in the central regions of the galaxies is crucial for effectively identifying GCs and unrelated background candidates that fall within the bright stellar emission near the galactic centers. Details regarding the ACS observations are logged in Table 3, and in Figure 2 we show mosaicked ACS images of the three galaxies in our sample with each of the  $202'' \times 202''$  observational fields highlighted.

For each galaxy, we first constructed a mosaicked image in the  $g_{475}$  band by aligning each of the images to a chosen reference observation and “drizzling” (Fruchter & Hook 2002) the images to the common frame. For NGC 3115, we first aligned ACS fields 3 and 4 (see annotations in Figure 2) to create a large central field that contained some overlapping areas common to the remaining ACS fields 1, 2, 5, and 6; these fields were subsequently aligned to the large central field. For NGC 3379 and NGC 3384, we aligned all observations to the central images (i.e., ACS fields 2 and 5 for NGC 3379 and NGC 3384, respectively). We performed field alignments using the Pyraf tools Tweakreg and Tweakback, which were available through the drizzlepac v.4.3.0<sup>18</sup> software package. Tweakreg and Tweakback identify sources that are common to each ACS image and a chosen reference image (here the galactic centers) and update the image headers once an astrometric solution is found. Given the small overlaps between images, we implemented only small shifts in right ascension and declination to align our images. In general,  $\approx 4$ –200 bright sources per image were used in the field alignments, and the resulting shifts and RMS residuals to the fits were  $\lesssim 10$  ACS pixels ( $\lesssim 0''.5$ ) and  $\lesssim 0.1$  pixels ( $\lesssim 0''.005$ ), respectively. After aligning the ACS fields, we constructed  $g_{475}$  mosaicked images using the astrodrizzle tool within drizzlepac. The astrodrizzle procedure uses the aligned, flat-field calibrated and charge-transfer efficiency corrected images to create a distortion-corrected mosaicked image with bad pixels and cosmic rays removed.

We repeated the above ACS image mosaicking procedure for the  $z_{850}$  band data, with the exception that all ACS observations of a given galaxy were aligned to the full  $g_{475}$  mosaicked image. The resulting two-colored mosaicked images are displayed in Figure 2 with the  $K$ -band galactic extents overlaid.

To construct source catalogs, we first searched each image mosaic using SExtractor (Bertin & Arnouts 1996). We chose the following SExtractor parameters: minimum detection area

of 5 pixels; detection and photometry analysis thresholds of  $3\sigma$ ; background grid of  $16 \times 16$  pixels with a filtering Gaussian of 2.5 pixels full width at half-maximum; and 32 deblending sub-thresholds. The SExtractor catalogs include some non-negligible contributions from background fluctuations and un-rejected cosmic rays (e.g., in chip gap regions where dithering makes cosmic-ray rejection difficult). For each galaxy, we constructed a master optical catalog, in which we required that sources be detected in both the  $g_{475}$  and  $z_{850}$  bands, using a matching radius of  $0''.5$ .

Within the central  $10''$ – $20''$  of the galactic centers, the stellar field backgrounds are very high, particularly in the  $z_{850}$  band, and our SExtractor searching does not yield source detections in these regions. Since we are unable to identify optical counterparts to X-ray sources (e.g., GCs and background sources) in these regions, we reject the X-ray sources in these regions from consideration when computing field LMXB XLFs. As we will describe in Section 5, these regions are also subject to significant X-ray point source confusion, which supports our choice to reject these regions. The sizes of these rejected regions have been tabulated in Column 8 of Table 1, and the fraction of the  $K$ -band luminosity contained within these regions, as measured by the  $K$ -band data, are provided in Column 10 in Table 1. Hereafter, we utilize  $K$ -band luminosities that have been corrected for the exclusion of these regions.

### 3.3. Astrometric Alignment of Chandra and HST Frames and Catalog Summaries

We further refined the absolute astrometry of our *Chandra* and *HST* data products and catalogs by registering them to either the Eighth Sloan Digital Sky Survey (SDSS) Data Release (DR8; Aihara et al. 2011) frame (NGC 3379 and 3384) or the United States Naval Observatory CCD Astrograph Catalog (UCAC2; Zacharias et al. 2000) frame when SDSS DR8 data were unavailable (NGC 3115). SDSS DR8 was astrometrically calibrated to UCAC2 frame; however, the SDSS DR8 reaches a much deeper limiting  $r$ -band magnitude of  $r_{\text{lim}} \approx 22.5$  (50% complete), compared to  $r_{\text{lim}} \approx 16$  for UCAC2, and is therefore our preferred optical reference frame.

To align our *HST* frames with reference optical frames (i.e., SDSS DR8 or UCAC2), we first cross-matched the *HST* master optical catalogs of each galaxy with the reference catalog using a  $1''.5$  matching radius. We then applied median astrometric shifts in right ascension and declination (total offsets ranged from  $0''.25$  to  $0''.56$  for the three galaxies) to the *HST* images and source catalogs to bring them into alignment with the reference frame. To align the *Chandra* catalogs and data products, we matched the *Chandra* main catalogs of each galaxy to their corresponding astrometry-corrected *HST* master optical catalogs using a matching radius of  $1''.5$ . Again, simple median shifts in right ascension and declination (offsets ranged from  $0''.17$  to  $0''.26$  for the three galaxies) were applied to the *Chandra* data products and catalogs to bring them into alignment with the *HST* and reference optical frames (by extension).

The final *HST* and *Chandra* image and catalog registrations have a  $1\sigma$  error of  $\approx 0''.12$ . Our further analyses are focused on sources that lie within the  $K$ -band extents of the galaxies outside the crowded nuclear regions (see Table 1). Within these galactic footprints, our main *Chandra* catalogs (see Section 3.1) contain 107, 134, and 47 X-ray sources for NGC 3115, 3379, and 3384, respectively, with the faintest FB detected sources reaching flux levels of 5.9, 7.9, and  $16 \times 10^{-17}$  erg cm<sup>-2</sup> s<sup>-1</sup>, respectively.

<sup>18</sup> See <http://drizzlepac.stsci.edu/> for details on drizzlepac.

**Table 3**  
*HST* Advanced Camera for Surveys (ACS) Observation Log

Galaxy	Field Number	Obs. Start (UT)	Exposure Time (s)		Line Dither Pattern		
			(F475W)	(F850LP)	$N_{\text{pts}}$		Spacing (arcsec)
					(F475W)	(F850LP)	
NGC 3115	1	2012 Mar 7, 02:49	824	1170	2	3	3.011
	2	2012 Mar 7, 04:25	824	1170	2	3	3.011
	3	2012 Mar 7, 06:14	722	1137	2	4	3.011
	4	2012 Mar 7, 08:06	824	1170	2	3	3.011
	5	2012 Mar 9, 17:05	824	1170	2	3	3.011
	6	2012 Mar 10, 00:07	824	1170	2	3	3.011
NGC 3379	2	2010 Mar 25, 04:08	760	1285	2	3	0.145
	3	2010 Apr 1, 00:38	754	1275	2	3	0.145
	4	2010 Apr 1, 02:14	754	1275	2	3	0.145
	5	2010 Apr 1, 03:50	754	1275	2	3	0.145
	6	2010 Apr 1, 05:26	754	1275	2	3	0.145
	6	2010 Apr 1, 05:26	754	1275	2	3	0.145
NGC 3384	4	2012 Apr 10, 14:30	780	1305	2	3	2.994
	5	2012 Apr 18, 08:59	800	1290	2	3	2.994
	6	2012 Apr 14, 03:06	780	1305	2	3	2.994

The optical limits of our *HST* catalogs vary substantially across the galactic footprints due to large background gradients from the galactic stellar fields. Within the galactic footprints (after excluding the inner regions specified in Table 1), our optical catalogs contain 582, 819, and 1125 total sources, which imply source densities of 64.8, 30.2, and 57.9 arcmin<sup>-2</sup> for NGC 3115, 3379, and 3384, respectively. As we will point out later, the factor of  $\approx 2$  times lower source density for NGC 3379 is also evident in the background X-ray number counts and is may be due to cosmic variance on the (small) size scale of the galactic footprints (see Section 5.3). Within the galactic footprints, we find that the  $g_{475}$ -band limiting depths of our catalogs is deepest in the innermost regions (outside the excluded radii given in Column 8 in Table 1) where the overlapping *HST* coverage generally contains a factor of  $\sim 2$  times deeper imaging than the galactic outskirts. Despite the deeper imaging in the central regions, we find that the  $z_{850}$ -band limiting depths are shallowest in the inner regions of the galaxy due to the enhanced background from the host galaxies in these regions. Specifically, in the inner regions of the galaxies, we find  $5\sigma$  limiting depths of  $g_{475}^{\text{lim}} \approx (26.0, 26.0, 26.3)$  and  $z_{850}^{\text{lim}} \approx (24.5, 24.5, 24.7)$  for NGC 3115, 3379, and 3384, respectively. In the outer regions, the respective  $5\sigma$  limiting depths are  $g_{475}^{\text{lim}} \approx (25.6, 25.6, 26.0)$  and  $z_{850}^{\text{lim}} \approx (24.9, 24.9, 25.1)$ .

#### 4. X-RAY SOURCE CLASSIFICATION

For each galaxy, we cross-correlated our astrometry-corrected *Chandra* main catalogs with our *HST* ACS optical master catalogs to identify likely counterparts to a subset of the X-ray point sources. An optical source was considered to be a likely counterpart if its position was located within the 95% confidence radius  $r_{95}$  of the X-ray source. The size of  $r_{95}$  depends on both net source counts and positional offset from the exposure-weighted mean aim point; these dependencies were calculated following Equation (12) of Kim et al. (2007). In total, we found 34, 28, and 17 optical counterparts to the X-ray point sources that were within the galactic extents of NGC 3115, 3379, and 3384, respectively; these represent 32%, 21%, and 36% of the X-ray sources, respectively. For each galaxy, we estimated the total number of false matches expected, given our matching criteria. To do this, we first estimated the optical source density  $\rho_{\text{opt}}$  as a function of angular distance from the galactic centers.

The expected number of false matches was then calculated as  $N_{\text{false}} \approx \sum_i \rho_{\text{opt},i} \times \sum_j A_{ij}$ , where  $\rho_{\text{opt},i}$  is the density of optical sources in the  $i$ th annulus and  $A_{ij}$  is the area enclosed by the 95% confidence positional error circle of the  $j$ th source residing in the  $i$ th annulus. We estimate that  $N_{\text{false}} \approx 1.1, 2.4,$  and  $1.3$  for NGC 3115, 3379, and 3384, respectively. These values imply that  $\sim 6\%$  of the X-ray sources with optical counterparts could be false matches, which will not have a material effect on our results.

We expect that optical counterparts to the X-ray sources will fall in one of two broad categories: LMXBs in GCs (expected to have  $z_{850} \approx 18\text{--}24$  mag, safely above the sensitivity limits in Section 3.3) and unrelated background sources. Hereafter, we define unrelated background sources to comprise all X-ray sources that are not intrinsically related to the galaxies being studied here. This category therefore includes foreground Galactic stars, as well as background active galactic nuclei (AGNs) and galaxies. Given that the most optically luminous counterparts to field LMXBs are expected to be normal stars with  $g_{475}$  and  $z_{850}$  magnitudes well below our detection thresholds (e.g., luminous red giants will have  $z_{850} \gtrsim 28\text{--}31$  mag at the distances to our galaxies), we do not expect to detect optical counterparts to individual field LMXBs. We therefore consider X-ray sources without optical counterparts to be candidate field LMXBs.

For X-ray sources with optical counterparts, we performed basic source classifications using their optical colors and light-profile information. Optical sources were classified as likely GCs if they had (1) colors in the range of  $0.6 \leq g_{475} - z_{850} \leq 1.6$ , (2) absolute magnitudes (based on the distances to each galaxy) in the range of  $-12.5 \leq M_z \leq -6.5$ , (3) extended light profiles in either the  $g_{475}$  or  $z_{850}$  bandpasses, characterized as having SExtractor stellarity parameters  $\text{CLASS\_STAR} \leq 0.9$  or aperture magnitude differences  $m(r_1) - m(r_2) > 0.4$ , where apertures consist of circles with radii  $r_1 = 0''.25$  and  $r_2 = 0''.5$ , and (4) light profiles in both the  $g_{475}$  and  $z_{850}$  bands that were not too extended to be GCs, defined as  $m(r_1) - m(r_2) \leq 0.9$ . X-ray sources with optical counterparts that did not meet these criteria were classified as unrelated background objects.

In Figure 3, we show 10 random examples of X-ray sources in NGC 3379 classified as GC and unrelated background sources. We visually inspected images similar to those shown in Figure 3 for all optical counterparts in all three galaxies. We found that our adopted selection criteria yielded reasonably

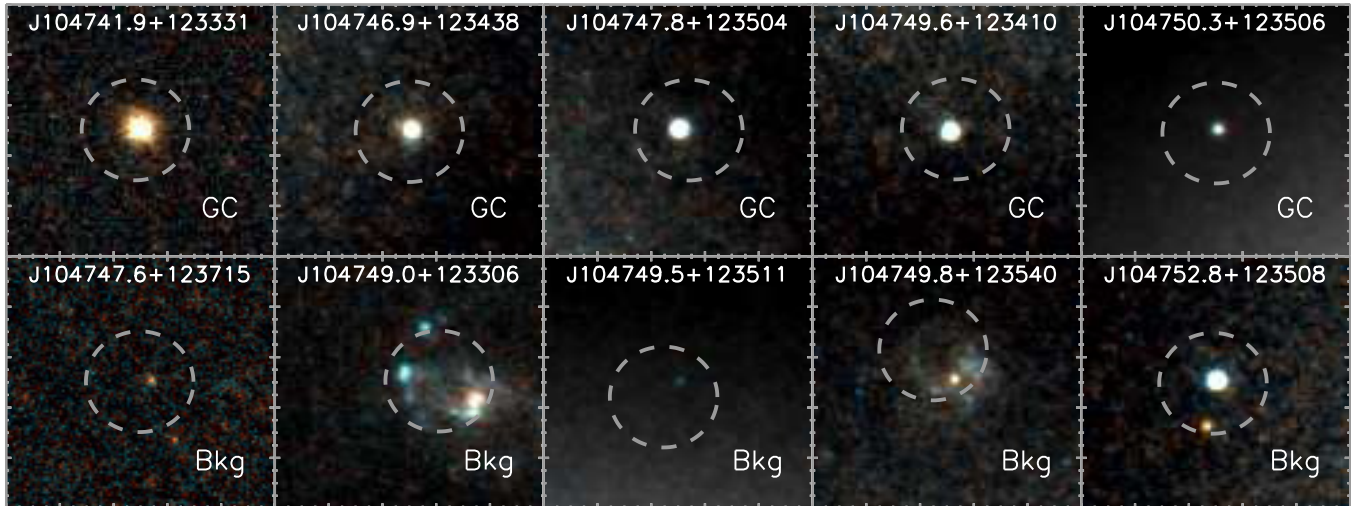


**Figure 3.** Sample ACS image postage stamps of X-ray-detected GCs (top panels) and unrelated background source (bottom panels) candidates in NGC 3379. Our optical source counterpart classification criteria are described in Section 4. Each postage stamp is centered on the optical source position and spans a  $2''.5 \times 2''.5$  region. For scaling purposes, we have included a circle with  $1''$  radius centered on the location of the X-ray source.

**Table 4**  
Summary of X-ray Source Classifications in Galaxy Footprints

Galaxy (1)	$N_{\text{tot}}$ (2)	$N_{\text{nuc}}$ (3)	$N_{\text{GC}}^{\text{LMXB}}$ (4)	$N_{\text{bkg}}$ (5)	$N_{\text{field}}^{\text{LMXB}}$ (6)
NGC 3115	153	46	25	9	73
NGC 3379	151	17	10	18	106
NGC 3384	65	18	3	14	30

**Notes.** Column 1: galaxy name. Column 2: total number of X-ray sources detected within the galaxy footprint, including the nuclear regions. Column 3: number of nuclear sources that were excluded from XLF computations (see Sections 3.2 and 5.2 for explanation and justification). After excluding the nuclear sources, Columns 4–6 provide the number of X-ray-detected sources classified as GC, unrelated background, and field LMXB candidates, respectively.

well segregated samples of GCs and unrelated background sources with few sources where the classifications are obviously incorrect. Furthermore, the inferred 0.5–8 keV luminosities of the GC counterparts were all less than  $L_X \approx 7 \times 10^{38} \text{ erg s}^{-1}$ , which is well within the expected range for GC LMXBs. We note that it is likely that a small minority of sources will have incorrect source classifications (e.g., faint sources with poor constraints on spatial properties); however, we do not expect these misclassifications to have any material effects on our conclusions. We also note that our ability to identify and separate GC LMXBs from field LMXBs is dependent on the completeness of our GC catalogs. Using the full *HST* catalogs, we constructed observed optical luminosity functions (i.e., number of detected sources per magnitude as a function of absolute magnitude  $M_z$ ) for sources detected within the galactic footprints. For all three galaxies, we found steadily rising number counts with decreasing  $M_z$  down to limits of  $M_z^{\text{lim}} \approx -5.0$  to  $-5.5$  before incompleteness began to affect source detection. As discussed above, GCs were selected to have  $-12.5 \leq M_z \leq -6.5$ , boundaries that are well above the highly complete limits. Our observed GC optical luminosity functions are consistent with those of the Milky Way, which to first order can be described as a Gaussian with peak luminosity at  $M_z \approx -7.9 \text{ mag}$  and  $\sigma \approx 1.3 \text{ mag}$  (Harris 1991). We therefore expect our GC selections to be highly complete.

In Table 4, we summarize our optical source categorizations for the X-ray sources. As discussed above, we have excluded

from consideration sources that were within small regions of the galactic centers due to the very bright stellar fields in these regions (see Section 3.2). The number of excluded sources has been provided in Column 3 of Table 4. Within the acceptable regions of the galaxy extents, we find 30–106 field LMXBs and 3–25 GC LMXBs per galaxy. In the sections below, we describe our procedure for generating LMXB XLF populations and present our resulting XLFs.

## 5. X-RAY LUMINOSITY FUNCTION COMPUTATION AND FITTING

We chose to compute XLFs in the FB (0.5–8 keV) to make direct comparisons with recent XLF studies of early-type galaxies (e.g., Zhang et al. 2012). Use of the FB for identifying X-ray point sources is appropriate for our early-type galaxy sample, since these galaxies have negligible contamination from hot gas (see, e.g., Figure 1) and little absorption at  $\lesssim 1 \text{ keV}$  from cold interstellar gas and dust. To compute XLFs for each of our galaxies, we made use of the FB-detected sources in the main *Chandra* catalogs presented in Section 3.1. Spatial variations in X-ray sensitivity, due to variations in local backgrounds, PSFs, effective exposures (e.g., chip gaps and bad pixels and columns), and source crowding, combined with incompleteness can have significant effects on the shape of the XLFs at X-ray luminosities that are within a factor of  $\approx 10$  of the detection limits. These effects need to be accounted for to properly compute the XLFs. Our approach, described in detail below, is to fit the *observed* XLFs with models of the *intrinsic* LMXB XLFs convolved with completeness functions derived from simulations.

### 5.1. X-Ray Background and Sensitivity Maps

Our first step in computing completeness functions was to construct FB background and sensitivity maps for each of the three galaxies in our sample. Background maps were constructed by first masking out all X-ray point sources within the merged FB images using circular masking regions of size 1.1 times the radius that encloses 99% of the PSF. These masking regions were computed and utilized by AE in the process of computing local background estimates for the point sources. After masking out the point sources, we filled the masked regions with Poisson noise that was characteristic of the local backgrounds as computed by AE. The background maps

enabled us to create sensitivity maps, which contain pixel-by-pixel estimates of the minimum number of counts  $s_{\min}$  that a hypothetical source would need to be detected given the local background. To compute  $s_{\min}$  at each location in a given image, it is necessary to estimate local values of  $b_{\text{src}}$  and  $b_{\text{ext}}$  (via Equation (1)) that are similar to those that would be estimated following the AE approach used for the X-ray-detected sources. Unfortunately, the AE procedure for extracting these values at every location in the image is computationally prohibitive, since source photometry is performed on an observation-by-observation basis using computationally intensive ray-tracing algorithms to generate local PSFs and approximations to the 90% EEf PSF contours. To overcome this issue, we estimated  $b_{\text{src}}$  by extracting background counts from the background maps using circular apertures with sizes that encompass the 90% EEf for a point source. Appropriate values of  $b_{\text{ext}}$  were estimated at each location (pixel) by extracting the maximum value of  $b_{\text{ext}}$  from the main *Chandra* catalogs for sources with off-axis angles  $\theta = \theta_p \pm 0.25$ , where  $\theta_p$  is the pixel off-axis angle. Given values of  $b_{\text{src}}$  and  $b_{\text{ext}}$ , we numerically solved the relation  $P(x \geq s_{\min}) = 0.004$  (i.e., Equation (1)) to obtain  $s_{\min}$  at each image location. In this manner, we constructed a spatial sensitivity map consisting of  $s_{\min}$  values.

### 5.2. X-Ray Completeness Functions

The above maps allow us to determine spatially whether a source would have been detected for a given number of total counts. However, these maps alone cannot directly be used to assess source completeness and encapsulate subtleties related to our complex selection process (i.e., *wavdetect* plus AE pruning) and source confusion in crowded regions. To assess better source detection completeness as a function of net source counts for each *Chandra* data set, we made use of simulated data sets and a Monte Carlo procedure that replicated the source detection and pruning processes that were used to create our source catalogs.

We began by generating 800 mock FB images for each galaxy with 35 X-ray sources artificially added to the original FB images. Ideally, we would have generated more mock images with only one X-ray source implanted in each mock image, so that the confusion properties would not be changed by the addition of sources. However, we found empirically that the addition of 35 sources per image both avoids having any non-negligible effect on the source confusion properties of the original images and allows for 35 times more efficient execution of the simulation process. For each X-ray source added to a given mock image, we assigned random right ascension and declination values that were probabilistically offset from the galaxy nucleus in accordance with the offset distribution of the main *Chandra* catalog. Each X-ray source was given a random number of counts between  $\approx 1$  and 100 counts. The counts from each source were added to the simulated image canvases using the *marx*<sup>19</sup> (ver. 4.5) ray-tracing code. In this procedure, the PSF of each source was modeled assuming a roll angle and aim point that were selected from one of the galaxy Obs. IDs (Table 2). Selection of the roll angle and aim point for each source was done probabilistically with the probability of selection being directly proportional to the exposure time of each of the observations.

For each galaxy, we performed circular aperture photometry on the 28,000 mock X-ray sources (i.e., 35 sources in each of

the 800 mock images) using a circular aperture with a radius encompassing  $\approx 90\%$  of the encircled energy. The number of counts measured for each source was then compared with the number of counts needed for a source detection from the sensitivity maps to see if it satisfied the detection criterion adopted in Equation (1). We then searched each of the 800 mock images using *wavdetect* at a false-positive probability threshold of  $10^{-5}$  and made *wavdetect* source catalogs for each image. We considered a simulated source to be “recovered” if (1) it was detected in the *wavdetect* runs, (2) the total number of counts exceeded the value required for a detection based on the sensitivity maps, and (3) the net counts derived were within  $3\sigma$  of the known input counts. Criterion (3) was adopted to account for source confusion since sources that are significantly confused with brighter sources in the original image will have an excess of source counts due to the unrelated source. We consider such sources to not be recovered.

Our simulations revealed that the central  $\approx 10''$ – $15''$  of the three early-type galaxies suffer catastrophic source confusion due to a high density of bright X-ray sources in the nuclear regions. As discussed in Section 3.2, these regions were considered problematic from an optical perspective, since the bright emission associated with the stellar fields made it impossible to identify potential GC and unrelated background candidates. These regions are problematic from the X-ray perspective because (1) it is not possible to recover accurately the true X-ray luminosity distributions of the sources in these regions, (2) the X-ray point sources may be formed via dynamical interactions in the high stellar density environments (e.g., Voss & Gilfanov 2007; Zhang et al. 2011), which are a different formation channel from the *field* LMXBs that we are interested in studying here, and (3) among the X-ray point sources of a given galaxy may be a low-luminosity AGN that could contaminate the LMXB XLFs at the high-luminosity ends. These considerations further support our choice to exclude these regions from our XLF computations below.

In Figure 4, we show the recovery fraction as a function of net source counts in radial bins for our three early-type galaxies. This plot was generated using circular annuli including only sources that were within the elliptical regions defined in Table 1; for the reasons discussed above, the exclusion region defined in Column 8 of Table 1 has not been shown. For NGC 3115 and 3379, we find that source recovery becomes more complete moving from the innermost annulus to the second innermost annulus. This is due to confusion becoming less severe at larger radii. The completeness again deteriorates going to even larger radii as the size of the PSF increases somewhat with radial distance (N.B., the exposure-weighted *Chandra* aimpoints are all within  $\approx 5''$  of the galaxy centers). For NGC 3384, confusion is not a strong issue for the innermost annulus; therefore, the completeness simply declines with radius.

### 5.3. Unrelated Background X-Ray Sources

One of the key strategies in our XLF computations is to identify directly and eliminate from consideration X-ray point sources that are associated with unrelated background objects. Direct optical identification of background X-ray sources is preferred over statistical methods, in which a background component is simply subtracted from the total XLFs, since the galaxies subtend only small solid angles on the sky ( $\lesssim 0.01$  deg<sup>2</sup>) and are subject to large variations in their background populations due to cosmic variance (e.g., Moretti et al. 2009). To test the efficacy of our background identifications, we constructed the

<sup>19</sup> See <http://space.mit.edu/exc/marx/> for *marx* simulator details.

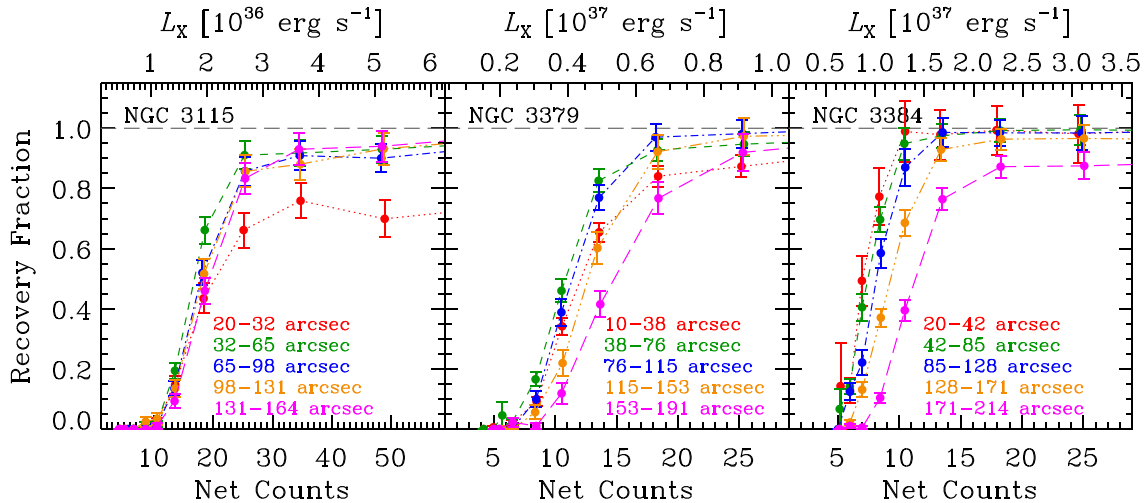


**Figure 4.** Fraction of recovered simulated sources as a function of net source counts for our three early-type galaxies (filled circles with  $1\sigma$  error bars). A simulated source was considered “recovered” if (1) the total number of on-source counts satisfied the binomial probability selection criterion of Equation (1), (2) the source was detected by *wavdetect* using a false-positive probability threshold of  $10^{-5}$ , and (3) the source had net counts that were within  $3\sigma$  of the input counts (required to identify confused sources). Each color represents a different offset range from the nuclear position, as annotated in each plot. Our best-fit models have been plotted as dashed curves. For a complete description of our simulations, see Section 5.2.

(A color version of this figure is available in the online journal.)

X-ray number counts ( $\log N - \log S$ ; the number of X-ray sources per unit area  $N$  with X-ray flux brighter than  $S$ ) relations for each of the three galaxies (and the combined sample) using the X-ray sources classified as unrelated background objects (see Section 4). For a given galaxy, we limited this calculation to a flux regime in which we could have detected sources across  $\approx 75\%$  of the galactic extent.

Figure 5 shows the  $\log N - \log S$  for the unrelated background sources in the early-type galaxy footprints (as well as the total galaxy sample) compared with expectation based on extragalactic blank-field X-ray surveys (e.g., Georgakakis et al. 2008). It is apparent that the number counts for unrelated background sources for NGC 3115 and 3384 are in good agreement with the expectation, while the NGC 3379 number counts fall a factor of  $\approx 2.5$ – $3$  times below the expectation across the full X-ray flux range. We expect that our optical identification and classification process will be most complete and accurate at bright fluxes ( $f_{0.5-8\text{ keV}} \gtrsim \text{few} \times 10^{-15} \text{ erg cm}^{-2} \text{ s}^{-1}$ ) where unrelated background counterparts are likely to be relatively unobscured AGNs with bright optical counterparts (e.g., Steffen et al. 2006; Xue et al. 2011). Since the deficit of X-ray sources in NGC 3379 is apparent at these high fluxes, it is likely that the deficit is real. As noted in Section 3.3, NGC 3379 also has a factor of  $\approx 2$  deficit in the source density of detected optical sources, lending strong support to this conclusion. Given the areal coverage of NGC 3379, we would expect cosmic variance at a level of  $\approx 30\%$ – $35\%$  (see Moretti et al. 2009). Therefore the factor of  $\gtrsim 2$  deficit for NGC 3379, if due to cosmic variance, would represent a  $\gtrsim 3\sigma$  deviation from the expected value (assuming the area-dependent cosmic variance distribution is symmetric and Gaussian).

The above number counts analysis suggests that the majority of unrelated X-ray background sources are likely to be classified as such by our procedure. In our computations of LMXB XLFs, described below, we remove unrelated background X-ray sources and do not try to correct for remaining contributions from unrecovered background X-ray sources. In the faint X-ray flux regime, where our recovery process is expected to be the least complete, background X-ray sources not

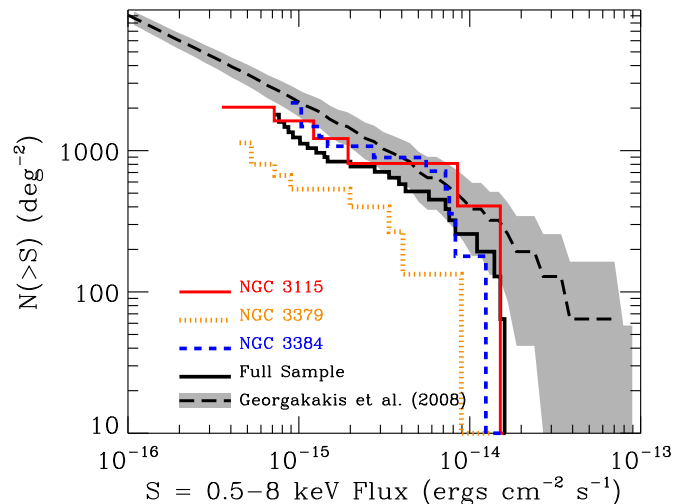


**Figure 5.** 0.5–8 keV number counts measurement for X-ray sources within the galactic footprints of our early-type galaxies that were optically classified as unrelated background objects (see annotations). For comparison, we show the expected number counts of unrelated background objects (dotted curve), and  $1\sigma$  error envelope (grey region), based on number counts from extragalactic X-ray surveys (Georgakakis et al. 2008). This comparison indicates that we are able to identify the majority of unrelated background X-ray sources using our methods. The deficit of number counts in NGC 3379 may be due to cosmic variance (see discussion in Section 5.3).

(A color version of this figure is available in the online journal.)

classified as such are greatly outnumbered by field LMXBs and therefore unlikely to have material effects on our results.

#### 5.4. X-Ray Luminosity Function Fitting

For each galaxy, we constructed *observed XLFs* using the FB-detected sources in the main *Chandra* catalogs that were within the galactic footprints (excluding sources in the near vicinities of the galactic nuclei; see Column 8 of Table 1). For each galaxy, we chose to construct and study the XLFs for three LMXB population categories, including GC plus field (total) LMXBs, field LMXBs, and GC LMXBs. However, for NGC 3384, we found only three GC LMXB candidates, which

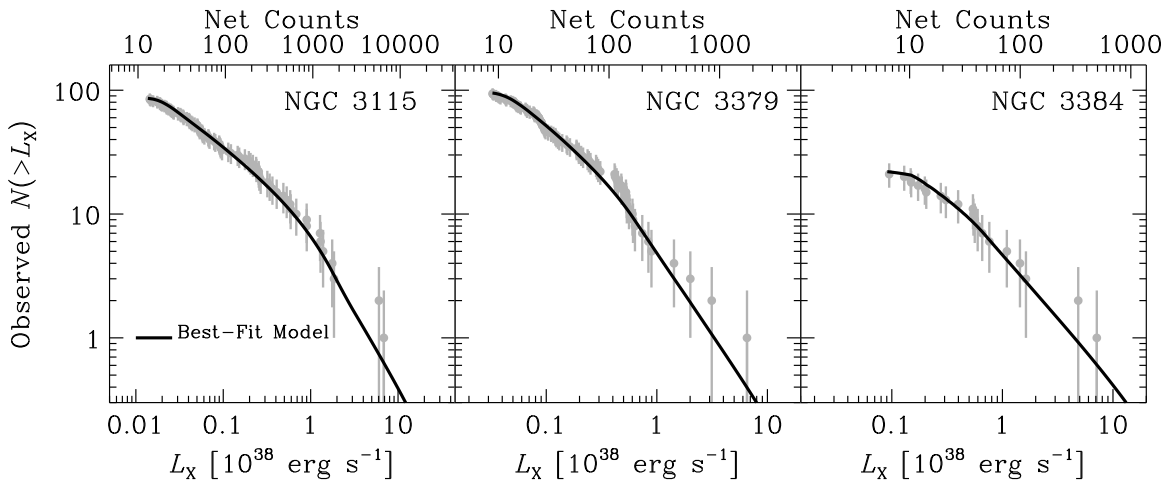


**Figure 6.** Cumulative observed X-ray luminosity functions ( $N(> L_X)$ ; thick black curves) for the GC plus field LMXB populations of the three early-type galaxies in our sample. Each observed XLF (gray circles with  $1\sigma$  Poisson error bars) includes X-ray-detected point sources within the extent of the galaxy after excluding unrelated background sources and sources within the central nuclear regions (see text). The XLFs were fit using an intrinsic XLF model convolved with our completeness functions following the procedure described in Section 5.4.

were all undetected in the FB, and therefore did not attempt to construct their GC LMXB XLF. In all cases, we excluded sources with optical counterparts classified as unrelated background objects. For illustration, we have displayed the cumulative observed XLFs (i.e.,  $N(> L_X)$ ) for the GC plus LMXB populations in Figure 6 (gray points with error bars).

For each of the three LMXB sub-populations, we modeled *intrinsic* XLFs using a broken power-law form that followed

$$dN/dL_X = \begin{cases} K(L_X/L_{\text{ref}})^{-\alpha_1} & (L_X \leq L_b) \\ K(L_b/L_{\text{ref}})^{\alpha_2-\alpha_1}(L_X/L_{\text{ref}})^{-\alpha_2} & (L_X > L_b), \end{cases}$$

where  $K$  is the normalization at reference luminosity  $L_{\text{ref}} \equiv 10^{38} \text{ erg s}^{-1}$ ,  $\alpha_1$  is the faint-end slope,  $L_b$  is the break luminosity, and  $\alpha_2$  is the bright-end slope.

We chose to model the observed XLFs using a forward-fitting approach, in which we convolved an appropriately weighted completeness function with our model XLFs before fitting to the observed XLFs. As demonstrated in Section 5.2 and Figure 4, our X-ray completeness to sources depends upon their offsets from the galactic centers. For a given galaxy, we therefore statistically weighted the contributions from model XLFs at each annulus according to the observed distributions of X-ray point sources to obtain the galaxy-wide weighted completeness function  $\xi(L_X)$ . Here we utilized only luminous X-ray sources in regimes where our point source populations are highly complete at all offsets from the galactic centers to determine the annular weightings. Formally, we computed  $\xi(L_X)$  using the following relation:

$$\xi(L_X) = \sum_i f_{\text{recov},i}(L_X) \times w_i, \quad (2)$$

where  $f_{\text{recov},i}(L_X)$  is the recovery-fraction curve for the  $i$ th annular bin and  $w_i$  is the fraction of total number of galaxy-wide sources within the  $i$ th annular bin based on the observed point-source distributions.

Using the *sherpa* modeling and fitting package available through *ciao*, we modeled each observed XLF using a multiplicative model

$$dN/dL_X(\text{observed}) = \xi(L_X)dN/dL_X(\text{model}). \quad (3)$$

For a given subsample of sources, we constructed the observed  $dN/dL_X(\text{observed})$  using a very small constant bin of  $\delta L_X$

spanning the minimum luminosity of the subsample to 10 times the maximum luminosity. Therefore the vast majority of bins contained zero sources up to a maximum of three sources. We evaluated the goodness of fit for our double power-law models using the Cash statistic (*cstat*; Cash 1979). We tested to see if in any cases a single power-law provided a statistically superior fit over the broken power-law, but were unable to find any such cases. We did find that for the field LMXB XLF in NGC 3115, the best-fitting broken power-law produced an effectively infinite high-luminosity slope ( $\alpha_2$ ) beyond the most luminous detected source. For this subclass, we utilized a single power-law with a high-luminosity cut-off (see Table 5). In Figure 6, we display the observed XLFs and best-fitting observed and intrinsic XLF models for the GC plus field LMXB populations for our three early-type galaxies. In Table 5, we tabulate the best-fit parameters and  $1\sigma$  errors for fits to the GC plus field LMXBs, field LMXBs, and GC LMXBs.

## 6. RESULTS

In Figure 7, we show the  $L_K$ -normalized cumulative LMXB XLFs ( $N(> L_X)/L_K$ ) for our early-type galaxies for GC plus field and field LMXB populations. The XLFs displayed in Figure 7 have been corrected for completeness, near the luminosity limits of each galaxy, using the completeness corrections derived from our best-fitting XLFs (see Section 5.4). We find that the GC plus field LMXB XLFs (Figure 7(a)) for all three galaxies appear to be similar in normalization and shape across  $L_X \approx 10^{37}$ – $10^{39} \text{ erg s}^{-1}$ . These estimates are in good agreement with the best-fit XLFs derived by Zhang et al. (2012) for a sample of 20 massive early-type galaxies (gray curve). However, when we remove the contributions from GC LMXBs, we observe significant galaxy-to-galaxy variations in the resulting field LMXB XLFs.

In Figure 7(b), we display the field LMXB XLF. We find that the shapes and normalizations of the field LMXB XLFs are similar for the two old early-type galaxies, NGC 3115 and 3379, with some differences becoming apparent at  $L_X \lesssim (2\text{--}4) \times 10^{37} \text{ erg s}^{-1}$ . For both of the old early-type galaxies, we observe sharp declines in the field LMXB XLFs above  $L_X \approx (0.5\text{--}1) \times 10^{38} \text{ erg s}^{-1}$ . By contrast, the field LMXB XLF for the young early-type galaxy NGC 3384 is generally elevated compared to those of the old early-type galaxies and

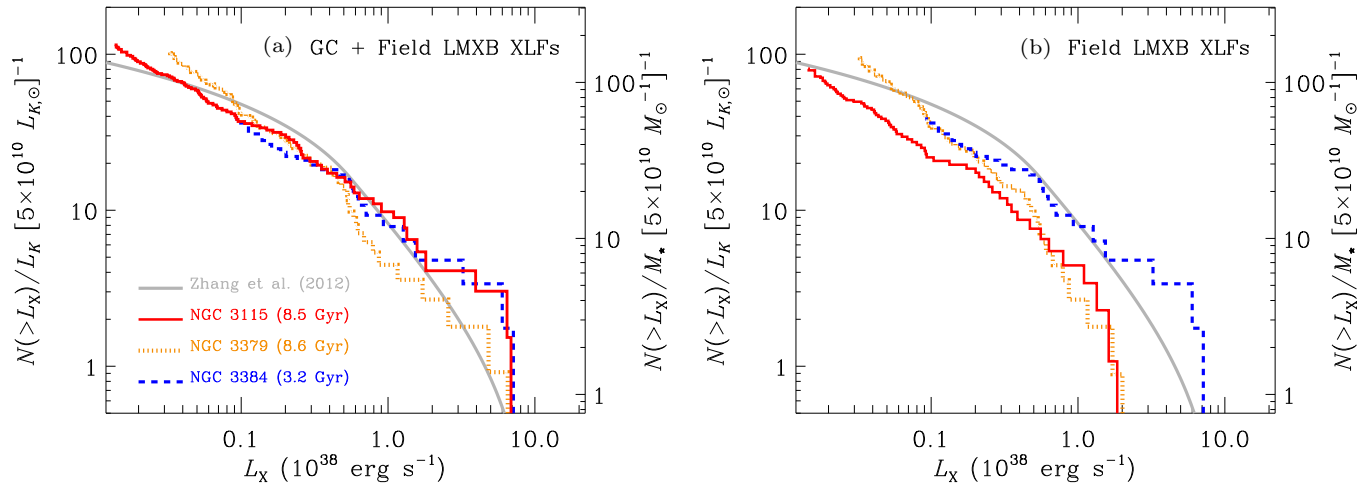


**Figure 7.** *K*-band–luminosity–normalized cumulative XLFs,  $N(>L_X)/L_K$ , for our early-type galaxies in two LMXB population categories: (a) GC plus field LMXBs and (b) field LMXBs. Each XLF has been summed down to an X-ray limit that is roughly 50% complete, and the displayed XLFs have been corrected for completeness following the methods described in Section 5.4. The three early-type galaxies have GC plus field (total) LMXB XLFs consistent with each other and previous results (Zhang et al. 2012). However, when looking at only the field LMXB XLF contribution, we find that the young early-type galaxy NGC 3384 has a more numerous and luminous field LMXB population than the old early-type galaxies NGC 3115 and 3379 (see Section 6 for more details).

(A color version of this figure is available in the online journal.)

**Table 5**  
Best-fit Parameters to X-ray Luminosity Functions (XLFs)

Galaxy	GC + Field (Total) LMXBs				Field LMXBs				GC LMXBs			
	$K$	$\alpha_1$	$\alpha_2$	$L_b$	$K$	$\alpha_1$	$\alpha_2$	$L_b$	$K$	$\alpha_1$	$\alpha_2$	$L_b$
NGC 3115	$6.8 \pm 1.8$	$1.5 \pm 0.1$	$2.2 \pm 0.7$	$1.76 \pm 0.02$	$4.6 \pm 1.2$	$1.5 \pm 0.1$	...	$1.853^{+0.391}_{-0.004}$ a	$2.8 \pm 1.2$	$1.3 \pm 0.2$	$1.7 \pm 0.6$	$1.76 \pm 0.19$
NGC 3379	$9.4 \pm 3.2$	$1.6 \pm 0.1$	$2.3 \pm 0.4$	$0.60 \pm 0.19$	$7.1 \pm 2.1$	$1.7 \pm 0.1$	$3.3 \pm 1.1$	$0.84 \pm 0.17$	$4.6 \pm 5.1$	$0.6 \pm 0.4$	$1.7 \pm 0.4$	$0.41 \pm 0.26$
NGC 3384	$6.1 \pm 3.1$	$1.3 \pm 0.4$	$2.0 \pm 0.4$	$0.68 \pm 0.23$	$6.1 \pm 3.1$	$1.3 \pm 0.4$	$2.0 \pm 0.4$	$0.68 \pm 0.23$	...	...	...	...

**Notes.**  $K$  and  $L_b$  are in units of  $(10^{38} \text{ erg s}^{-1})^{-1}$  and  $10^{38} \text{ erg s}^{-1}$ , respectively. All errors are  $1\sigma$  and are based on the fitting procedure described in Section 5.4. For NGC 3384, all FB detected LMXBs have been classified as field candidates; therefore the GC plus field and field only fit parameters are identical.

a The best-fit model to the field LMXB XLF for NGC 3115 was a single power-law with normalization  $K$ , slope  $\alpha_1$ , and high-luminosity cut at the quoted  $L_b$  value.

includes an extension to higher X-ray luminosities ( $L_X \approx 7 \times 10^{38} \text{ erg s}^{-1}$ ); however, as is apparent from Figure 7(b), the cumulative field XLF of NGC 3384 approaches that of NGC 3379 at  $L_X \approx 3 \times 10^{37} \text{ erg s}^{-1}$ . A similar excess of luminous ( $L_X > 5 \times 10^{38} \text{ erg s}^{-1}$ ) LMXBs in young early-type galaxies was previously observed by Kim & Fabbiano (2010) and Zhang et al. (2012) using GC plus field LMXB populations. Our analysis shows that this excess may apparently be attributed to a strong excess in *field* LMXBs, and the removal of GC LMXBs seems to amplify this excess of bright X-ray sources. This result clearly illustrates that *HST* data are crucially needed to identify directly LMXB counterparts and provide meaningful tests of population synthesis models. By selection, the galaxies in our sample have relatively low  $S_N$  ( $S_N \lesssim 3$ ), so the large elliptical galaxies that have been studied well thus far will contain even larger contributions from GC LMXBs.

In Figure 8, we display the GC LMXB cumulative XLFs normalized by  $L_K$  and  $S_N$  ( $N(>L_X)/L_K/S_N$ ). We note that NGC 3384 had no GC LMXBs detected in the FB; we therefore show only the  $3\sigma$  upper limit to its GC XLF at the detection limit. From Figure 8, we see that the GC LMXB XLFs for NGC 3115 and 3379 appear to be broadly consistent in their shape and normalization; the upper limit on the GC LMXB XLF for NGC 3384 is consistent with the other galaxies. For the purpose of comparing XLF shapes, we have plotted in light gray  $N(>L_X)/L_K$  (without the  $S_N$  normalization) for the field LMXBs. We find that the GC LMXB XLFs of NGC 3115 and 3379 have significantly shallower slopes and extend to higher

X-ray luminosities than the field LMXB XLFs. This result is consistent with previous results that compared GC and field LMXB XLFs (e.g., Kim et al. 2009; Voss et al. 2009; Paolillo et al. 2011).

The above findings indicate that the young early-type galaxy NGC 3384 contains a more numerous and X-ray luminous population of field LMXBs per unit *K*-band luminosity (stellar mass) than the older early-type galaxies NGC 3115 and 3379 (see Section 6). Although the integrated X-ray luminosity per unit *K*-band luminosity  $L_X/L_K$  can be measured to high precision for the LMXB populations in the three galaxies in our sample, and our measurements clearly indicate that the field LMXB  $(L_X/L_K)_{\text{field}}$  is larger for NGC 3384 than for NGC 3115 and 3379, it is important to account for the fact that the  $L_X$  value for a given galaxy can be substantially influenced by the brightest few sources. If we consider the distribution of point-source luminosities as a realization of an underlying XLF, then we might expect large galaxy-to-galaxy variations in  $L_X/L_K$  simply due to “statistical noise” (see Gilfanov et al. 2004 for a detailed discussion on this issue). For example, a large sample of galaxies with identical underlying XLFs will contain a spread of  $L_X$  values due to this statistical noise.

To quantify how this statistical noise influences our results, we made use of a Monte Carlo technique to measure the expected standard deviation of  $L_X/L_K$  for a given XLF. For each of our LMXB populations in each galaxy, we constructed 20,000 simulated XLFs that contained distributions consistent with the best-fitting XLF model (see Section 5.4 and Table 5). For a given

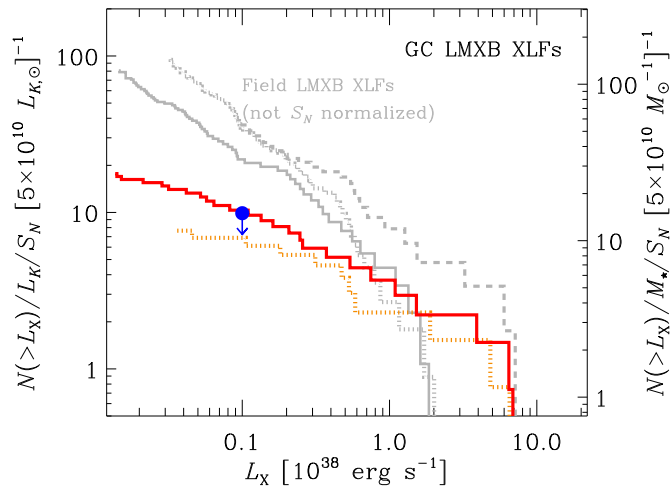


**Figure 8.** GC LMXB cumulative XLFs normalized by  $L_K$  and  $S_N$  (colored curves) with field LMXB cumulative XLFs, normalized by  $L_K$  only, displayed for comparison (gray curves). Linestyles and colors follow the same scheme as in Figure 7, with the exception of NGC 3384, for which we only obtain an upper limit on the GC cumulative XLF at the detection limit (filled blue circle with arrow). We find that when normalized by  $L_K$  and  $S_N$ , the GC LMXB XLFs are all consistent with each other in shape and normalization and have overall slopes shallower than the field LMXB XLFs.

(A color version of this figure is available in the online journal.)

simulation, we first computed the expected number of LMXBs that would have  $L_X \gtrsim 10^{36}$  erg s $^{-1}$  and perturbed this value using Poisson statistics. We then assigned  $L_X$  values to each of the sources probabilistically using the best-fitting XLF model as our underlying probability distribution function. Finally, the sources within a given simulation were summed to give an integrated  $L_X$  value. The resulting distribution of 20,000  $L_X$  values provided us with the effects of the statistical noise on our results. In Table 6, we have tabulated the integrated  $L_X$  and  $L_X/L_K$  values and their errors, which include the statistical noise, and in Figure 9(a), we have plotted the field LMXB  $(L_X/L_K)_{\text{field}}$  versus stellar age (and  $1\sigma$  errors) for the galaxies in our sample. We have found that the resulting errors on  $\log L_X$  values are well described by Gaussian functions, implying asymmetric  $L_X$  errors. Considering these errors, and following the error propagation methods described in Section 2.4.5 of Eadie et al. (1971), we find that the field LMXB  $(L_X/L_K)_{\text{field}}$  for NGC 3384 is a factor of  $2.0^{+1.7}_{-0.9}$  and  $3.0^{+2.5}_{-1.4}$  times higher than NGC 3115 and 3379, respectively.

## 7. DISCUSSION

Our results support a scenario in which the field LMXB X-ray luminosity per unit  $K$ -band luminosity  $(L_X/L_K)_{\text{field}}$  declines with increasing stellar age, as predicted by population synthesis models (filled circles in Figure 9(a)). In Figure 9(a) we have displayed the expected mass-weighted stellar age dependent  $(L_X/L_K)_{\text{field}}$  from the population synthesis models from Fragos et al. (2013b; dashed curve with gray shaded region). This curve was derived using Equation (4) of Fragos et al. (2013b) and an assumed  $M/L_K \approx 0.66 M_\odot/L_{K,\odot}$ , consistent with our galaxies. We find that the population synthesis models predict that galaxies with mass-weighted stellar ages of  $\approx 3.2$  Gyr will have  $(L_X/L_K)_{\text{field}}$  values that are a factor of  $\approx 3$  times higher than  $\approx 8.5$  Gyr galaxies, which is consistent with our finding. We note that the absolute scaling of our field LMXB  $(L_X/L_K)_{\text{field}}$  values appear to be a factor of  $\sim 1.5$ – $2$  times lower than the maximum likelihood model

**Table 6**  
Integrated X-ray Luminosities

Galaxy	$\log L_X$ (log erg s $^{-1}$ )	$\log L_X/L_K$ (log erg s $^{-1} L_{K,\odot}^{-1}$ )
GC + Field (Total)		
NGC 3115	$39.58 \pm 0.19$	$28.90 \pm 0.19$
NGC 3379	$39.51 \pm 0.12$	$28.75 \pm 0.12$
NGC 3384	$39.37 \pm 0.26$	$28.87 \pm 0.26$
Field		
NGC 3115	$39.08 \pm 0.10$	$28.40 \pm 0.10$
NGC 3379	$39.35 \pm 0.07$	$28.58 \pm 0.07$
NGC 3384	$39.37 \pm 0.26$	$28.87 \pm 0.26$
GC		
NGC 3115	$39.52 \pm 0.34$	$28.84 \pm 0.34$
NGC 3379	$39.17 \pm 0.50$	$28.40 \pm 0.50$

adopted in the Fragos models. However, it is important to note that these models were calibrated to match local total (i.e., GC plus field)  $(L_X/L_K)_{\text{total}}$  LMXB scaling relations, which as we have shown in this study, are affected somewhat by the GC LMXB populations. Furthermore, the range of statistically acceptable population synthesis models (i.e., the shaded region in Figure 9(a); see Fragos et al. 2013b for details) covers our field LMXB  $(L_X/L_K)_{\text{field}}$  values. Using the three  $(L_X/L_K)_{\text{field}}$  values derived from this study, we adjusted the normalization term in Equation (4) of Fragos et al. (2013b) to fit our results. Using  $\chi^2$  minimization, we found that a factor of  $\approx 1.6$  downward shift of the normalization would provide a reasonable fit to our data (solid curve in Figure 9(a)).

Our pilot study provides suggestive evidence that the X-ray emission from field LMXB populations declines with stellar age; however, it is absolutely critical to expand this study to a larger sample of early-type galaxies using comparable *Chandra* and *HST* imaging before we draw statistically robust conclusions. As we noted in Section 1, previous studies have found that the total (GC plus field)  $(L_X/L_K)_{\text{total}}$  increases with stellar age. In Figure 9(a), we have displayed the  $(L_X/L_K)_{\text{total}}$  versus age for the Boroson et al. (2011) sample. It is clear that indeed there is a positive correlation between  $(L_X/L_K)_{\text{total}}$  and stellar age; a Spearman rank test indicates that the correlation is significant at the  $>99.9\%$  confidence level. However, as pointed out by Zhang et al. (2012), this correlation is strongly influenced by a secondary correlation of GC  $S_N$  with stellar age (see Figure 9(b)). As discussed in Section 6, we have shown that the  $L_K$  and  $S_N$  normalized GC XLFs for the galaxies in our sample are consistent with each other, suggesting that the GC  $(L_X/L_K/S_N)_{\text{GC}}$  may be a “universal” quantity for early-type galaxies generally. A similar conclusion was reached by Irwin (2005), who determined the  $B$ -band luminosity normalized quantity  $(L_{0.3-10\text{keV}}/L_B/S_N)_{\text{GC}} = (2.72 \pm 0.47) \times 10^{29}$  erg s $^{-1} L_{B,\odot}^{-1}$  for a sample of 12 galaxies. If we assume  $L_X/L_{0.3-10\text{keV}} \approx 0.8$  and  $L_B/L_K \approx 0.18 L_{B,\odot}/L_{K,\odot}$ , appropriate for our X-ray binaries and galaxies, respectively, we can convert the Irwin (2005) relation to  $(L_X/L_K/S_N)_{\text{GC}} = (3.70 \pm 0.64) \times 10^{28}$  erg s $^{-1} L_{K,\odot}^{-1}$ . Using the data provided in Tables 1 and 6, we find that  $(L_X/L_K/S_N)_{\text{GC}} \approx 3.0^{+3.5}_{-1.6} \times 10^{28}$  erg s $^{-1} L_{K,\odot}^{-1}$  and  $1.9^{+4.2}_{-1.3} \times 10^{28}$  erg s $^{-1} L_{K,\odot}^{-1}$  for NGC 3115 and 3379, respectively, both formally consistent with the Irwin (2005) estimate.

Given the measurements of GC LMXB  $(L_X/L_K/S_N)_{\text{GC}}$  and correlations between GC plus field  $(L_X/L_K)_{\text{total}}$  and  $S_N$  with stellar age, we can roughly estimate how the field  $(L_X/L_K)_{\text{field}}$

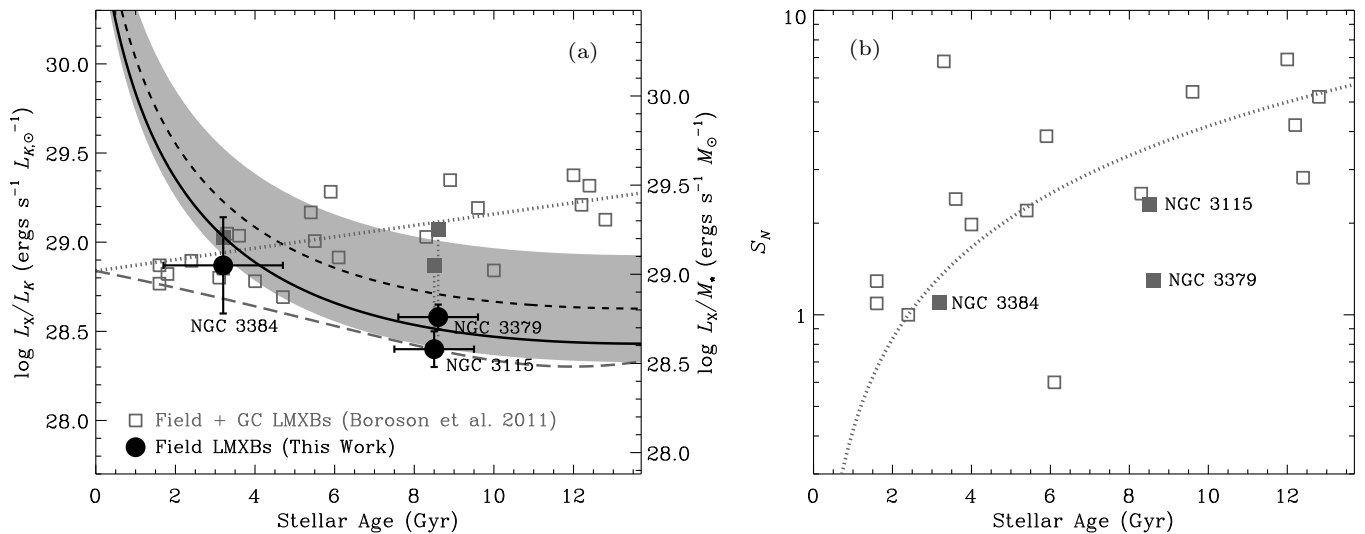


**Figure 9.** (a) Integrated LMXB X-ray luminosity per  $L_K$  vs. stellar age for the field LMXBs,  $(L_X/L_K)_{\text{field}}$ , in the three galaxies in our sample (filled circles with annotations) and the total (GC plus field) LMXBs,  $(L_X/L_K)_{\text{total}}$ , in the Borosen et al. (2011) sample (gray squares). The three filled gray squares indicate the Borosen et al. (2011)  $(L_X/L_K)_{\text{total}}$  values for the three galaxies in our sample. The dashed black curve and surrounding gray region is the expected relation and spread from the population synthesis models of Fragos et al. (2013b), and the solid curve shows the best-fit version of this curve renormalized to our data. The dotted gray curve is the best-fit relation to the GC plus field LMXB  $(L_X/L_K)_{\text{total}}$  vs. age data (i.e., the gray squares) and the long-dashed curve shows how this correlation would change after subtracting the expected contributions from GC LMXBs (see Equation (7) and discussion in Section 7 for details). (b) The observed relation between GC  $S_N$  and stellar age with the best-fitting model (dotted gray curve). We find that the apparent correlation in panel (a) between  $(L_X/L_K)_{\text{total}}$  and stellar age can be fully explained by contributions from GC LMXBs and the underlying correlation between GC  $S_N$  and stellar age shown in panel (b). Furthermore, the contributions from GC LMXBs could mask an underlying anticorrelation between  $(L_X/L_K)_{\text{field}}$  and stellar age (e.g., the long-dashed curve in panel (a)).

would be expected to scale with stellar age. This can be done by solving the following system of equations:

$$\log(L_X/L_K)_{\text{total}} \sim A + B t_{\text{age}}, \quad (4)$$

$$(L_X/L_K)_{\text{GC}} \sim C S_N, \quad (5)$$

$$S_N \sim D t_{\text{age}}, \quad (6)$$

$$\begin{aligned} (L_X/L_K)_{\text{field}} &= (L_X/L_K)_{\text{total}} - (L_X/L_K)_{\text{GC}}, \\ \rightarrow (L_X/L_K)_{\text{field}} &\sim 10^{A+B t_{\text{age}}} - C \times D t_{\text{age}}, \end{aligned} \quad (7)$$

where  $A$ ,  $B$ ,  $C$ , and  $D$  are constants. Using the Borosen et al. (2011) data presented in Figures 9(a) and (b), we determined  $A \approx 28.84 \log \text{erg s}^{-1} L_{K,\odot}^{-1}$ ,  $B \approx 0.032 \log \text{erg s}^{-1} L_{K,\odot}^{-1} \text{Gyr}^{-1}$ , and  $D \approx 0.42 \text{Gyr}^{-1}$ . The dotted gray curves in Figures 9(a) and (b) illustrate the best-fit solutions to Equations (4) and (6), respectively. If we adopt  $C \approx 3 \times 10^{28} \text{erg s}^{-1} L_{K,\odot}^{-1}$  (see above for justification) and insert this set of values into Equation (7), then we obtain an estimate for  $(L_X/L_K)_{\text{field}}$ , which we show as the long-dashed curve in Figure 9(a). This exercise illustrates that the positive correlation of  $(L_X/L_K)_{\text{total}}$  with stellar age is dominated by contributions from GC LMXBs and that it is possible to mask an underlying negative correlation between  $(L_X/L_K)_{\text{field}}$  and stellar age. We note, however, that the above calculation is very sensitive to the set of constants that are adopted. Although each of the constants above were derived directly from the data, it is possible to perturb a constant in a manner entirely consistent with the data and obtain a qualitatively different result. For example, if we adopted  $C = 2 \times 10^{28} \text{erg s}^{-1} L_{K,\odot}^{-1}$ , the value obtained for NGC 3379, we would find the long-dashed curve in Figure 9(a) to have a flat slope. Or if we adopted  $C = 4 \times 10^{28} \text{erg s}^{-1} L_{K,\odot}^{-1}$ , a value higher than but consistent with those obtained for NGC 3115

and 3379 and the Irwin (2005) result, the resulting  $(L_X/L_K)_{\text{field}}$  from Equation (7) would be negative at  $t_{\text{age}} > 6.7 \text{Gyr}$ . Therefore, the above calculation should be taken as a proof of concept and not a well constrained measurement of the stellar age dependence of  $(L_X/L_K)_{\text{field}}$ . To obtain an accurate measurement of how  $(L_X/L_K)_{\text{field}}$  varies with stellar age will require direct measurements of the field LMXB populations in a larger sample of galaxies using the combination of *HST* and *Chandra* data sets. Obtaining such an accurate measurement will be important for constraining X-ray binary population synthesis models. For example, the above inferences for how  $(L_X/L_K)_{\text{field}}$  changes with stellar age (i.e., the long-dashed curve in Figure 9) appears flatter than the current X-ray binary population synthesis predictions at the youngest stellar ages. Direct measurements of  $(L_X/L_K)_{\text{field}}$  for several galaxies are required to show whether this is indeed the case and whether these predictions will need to be revised.

## 8. SUMMARY

We have utilized deep *Chandra* and *HST* observations of the three nearby early-type galaxies NGC 3115, 3379, and 3384 to identify and study sub-populations of LMXBs that are found in the galactic field environments. Our galaxy sample was selected to span a large range of stellar age ( $\approx 3$ –10 Gyr) so that we could measure how the emission from field LMXBs depends on stellar population ages. Our results can be summarized as follows:

1. We find that LMXBs formed dynamically in GCs and unrelated background X-ray sources can significantly impact the overall XLF shapes and X-ray power output from early-type galaxies, even in low- $S_N$  galaxies like the three sources studied here ( $S_N \lesssim 3$ ). This finding indicates that for studies of field LMXBs, it is critical to remove GC LMXBs and unrelated background sources using the combination of *HST* and *Chandra* data. This is especially the case for the majority of early-type galaxies that have been studied

in the literature, which have  $S_N \gtrsim 2$  (see Figure 7 and Sections 4 and 6).

2. After normalizing for stellar mass (via the  $K$ -band luminosity), we find that the field LMXB population in the young ( $\approx 3.2$  Gyr) galaxy NGC 3384 is more numerous and extends to higher luminosities than the older ( $\approx 8.5$  Gyr) galaxies NGC 3115 and 3379. This result is consistent with previous studies that have found a similar excess of luminous X-ray sources in young ( $\lesssim 6$  Gyr) versus old ( $\gtrsim 6$  Gyr) early-type galaxies (e.g., Kim & Fabbiano 2010; Zhang et al. 2012; see Figure 7(b), and Section 6).
3. Using the field LMXB populations in our galaxies, we measure the integrated  $(L_X/L_K)_{\text{field}}$  for NGC 3384 to be a factor of  $\approx 2$ –3 times higher than that found in NGC 3115 and 3379. This result is consistent with the trends expected from the X-ray binary population synthesis models published by Fragos et al. (2013a, 2013b), which predict that the  $(L_X/L_K)_{\text{field}}$  will be a factor of  $\approx 3$  times higher for galaxies with stellar ages of  $\approx 3$  Gyr compared to those with  $\approx 9$  Gyr (see Figure 9(a) and Sections 6 and 7).
4. We find that the GC LMXB XLFs for NGC 3115 and 3379 are consistent with each other when normalized by  $L_K$  and  $S_N$ . We did not detect enough GC LMXBs in NGC 3384 to study the shape of its GC LMXB XLF; given its low  $S_N$ , our lack of GC LMXB detections is not surprising. We constrained the mean GC LMXB  $(L_X/L_K/S_N)_{\text{GC}} \approx (2\text{--}3) \times 10^{28} \text{ erg s}^{-1} L_{K,\odot}^{-1}$  for these galaxies, in good agreement with past studies (Irwin 2005) (see Figure 8 and Sections 6 and 7).
5. Previous studies have found that the total GC plus field LMXB  $(L_X/L_K)_{\text{total}}$  was positively correlated with stellar age, which was considered an apparent conflict with population synthesis predictions. This observed correlation is largely driven by an underlying correlation between  $S_N$  and stellar age, which masks any underlying correlations of  $(L_X/L_K)_{\text{field}}$  with stellar age. We showed that if we consider our constraint on  $(L_X/L_K/S_N)_{\text{GC}}$  and the  $S_N$ –stellar age correlation, it is plausible that  $(L_X/L_K)_{\text{field}} = (L_X/L_K)_{\text{total}} - (L_X/L_K/S_N)_{\text{GC}}$  declines with increasing stellar age. However, a robust measurement of  $(L_X/L_K)_{\text{field}}$  versus age will only come from a detailed *Chandra* and *HST* study of the field LMXB populations from a larger sample of early-type galaxies (see Figure 9 and Sections 1, 6, and 7).

We thank the referee for providing thoughtful comments that have improved the quality of this paper. We thank Zhongli Zhang for providing data. We gratefully acknowledge financial support from *Chandra* X-ray Center grant G02-13107A, Space Telescope Science Institute grant GO-12760, and NASA ADP grant NNX13AI48G (B.D.L.). F.E.B. acknowledges support from Basal-CATA PFB-06/2007, CONICYT-Chile (grants FONDECYT 1101024, Gemini-CONICYT 32120003, “EMBIGGEN” Anillo ACT1101), and Project IC120009 “Millennium Institute of Astrophysics (MAS)” funded by the Iniciativa Científica Milenio del Ministerio de Economía, Fomento y Turismo. W.N.B. acknowledges ADP grant NNX10AC99G. G.R.S. is supported by an NSERC Discovery Grant. V.K. acknowledges support for this work from NASA ADP grant NNX12AL39G (sub-contract to Northwestern University)

## REFERENCES

- Aihara, H., Allende Prieto, C., An, D., et al. 2011, *ApJS*, **193**, 29
- Bekki, K., Yahagi, H., & Forbes, D. A. 2006, *ApJL*, **645**, L29
- Belczynski, K., Kalogera, V., & Bulik, T. 2002, *ApJ*, **572**, 407
- Belczynski, K., Kalogera, V., Rasio, F. A., et al. 2008, *ApJS*, **174**, 223
- Bell, E. F., McIntosh, D. H., Katz, N., & Weinberg, M. D. 2003, *ApJS*, **149**, 289
- Bertin, E., & Arnouts, S. 1996, *A&AS*, **117**, 393
- Borison, B., Kim, D.-W., & Fabbiano, G. 2011, *ApJ*, **729**, 12
- Brassington, N. J., Fabbiano, G., Blake, S., et al. 2010, *ApJ*, **725**, 1805
- Brassington, N. J., Fabbiano, G., Kim, D.-W., et al. 2008, *ApJS*, **179**, 142
- Brassington, N. J., Fabbiano, G., Zezas, A., et al. 2012, *ApJ*, **755**, 162
- Broos, P. S., Townsley, L. K., Feigelson, E. D., et al. 2010, *ApJ*, **714**, 1582
- Cash, W. 1979, *ApJ*, **228**, 939
- Colbert, E. J. M., Heckman, T. M., Ptak, A. F., Strickland, D. K., & Weaver, K. A. 2004, *ApJ*, **602**, 231
- David, L. P., Jones, C., Forman, W., Vargas, I. M., & Nulsen, P. 2006, *ApJ*, **653**, 207
- Eadie, W. T., Dryard, D., James, F. E., Roos, M., & Sadoulet, B. 1971, *Statistical Methods in Experimental Physics* (Amsterdam: North-Holland)
- Ellis, S. C., & O’Sullivan, E. 2006, *MNRAS*, **367**, 627
- Fabian, A. C., Pringle, J. E., & Rees, M. J. 1975, *MNRAS*, **172**, 15P
- Fabbiano, G. 2006, *ARA&A*, **44**, 323
- Fragsos, T., Kalogera, V., Belczynski, K., et al. 2008, *ApJ*, **683**, 346
- Fragsos, T., Lehmer, B., Tremmel, M., et al. 2013a, *ApJ*, **764**, 41
- Fragsos, T., Lehmer, B. D., Naoz, S., Zezas, A., & Basu-Zych, A. 2013b, *ApJL*, **776**, L31
- Freeman, P. E., Kashyap, V., Rosner, R., & Lamb, D. Q. 2002, *ApJS*, **138**, 185
- Fruchter, A. S., & Hook, R. N. 2002, *PASP*, **114**, 144
- Georgakakis, A., Nandra, K., Laird, E. S., Aird, J., & Trichas, M. 2008, *MNRAS*, **388**, 1205
- Gilfanov, M. 2004, *MNRAS*, **349**, 146
- Gilfanov, M., Grimm, H.-J., & Sunyaev, R. 2004, *MNRAS*, **351**, 1365
- Grimm, H.-J., Gilfanov, M., & Sunyaev, R. 2002, *A&A*, **391**, 923
- Harris, W. E. 1991, *ARA&A*, **29**, 543
- Hickox, R. C., & Markevitch, M. 2006, *ApJ*, **645**, 95
- Hills, J. G. 1976, *MNRAS*, **175**, 1P
- Hornschemeier, A. E., Brandt, W. N., Garmire, G. P., et al. 2001, *ApJ*, **554**, 742
- Irwin, J. A. 2005, *ApJ*, **631**, 511
- Jarrett, T. H., Chester, T., Cutri, R., Schneider, S. E., & Huchra, J. P. 2003, *AJ*, **125**, 525
- Juett, A. M. 2005, *ApJL*, **621**, L25
- Kainulainen, J. T., Alves, J. F., Beletsky, Y., et al. 2009, *A&A*, **502**, L5
- Kim, D.-W., & Fabbiano, G. 2004, *ApJ*, **611**, 846
- Kim, D.-W., & Fabbiano, G. 2010, *ApJ*, **721**, 1523
- Kim, D.-W., Fabbiano, G., Brassington, N. J., et al. 2009, *ApJ*, **703**, 829
- Kim, D.-W., Fabbiano, G., Kalogera, V., et al. 2006, *ApJ*, **652**, 1090
- Kim, M., Kim, D.-W., Wilkes, B. J., et al. 2007, *ApJS*, **169**, 401
- Lehmer, B. D., Alexander, D. M., Bauer, F. E., et al. 2010, *ApJ*, **724**, 559
- Lehmer, B. D., Brandt, W. N., Alexander, D. M., et al. 2007, *ApJ*, **657**, 681
- McDermid, R. M., Emsellem, E., Shapiro, K. L., et al. 2006, *MNRAS*, **373**, 906
- Moretti, A., Pagani, C., Cusumano, G., et al. 2009, *A&A*, **493**, 501
- Norris, M. A., Sharples, R. M., & Kuntschner, H. 2006, *MNRAS*, **367**, 815
- O’Sullivan, E., Forbes, D. A., & Ponman, T. J. 2001, *MNRAS*, **328**, 461
- Paolillo, M., Puzia, T. H., Goudfrooij, P., et al. 2011, *ApJ*, **736**, 90
- Sánchez-Blázquez, P., Forbes, D. A., Strader, J., Brodie, J., & Proctor, R. 2007, *MNRAS*, **377**, 759
- Sánchez-Blázquez, P., Gorgas, J., Cardiel, N., & González, J. J. 2006, *A&A*, **457**, 809
- Shapiro, K. L., Falcón-Barroso, J., van de Ven, G., et al. 2010, *MNRAS*, **402**, 2140
- Spergel, D. N., Verde, L., Peiris, H. V., et al. 2003, *ApJS*, **148**, 175
- Steffen, A. T., Strateva, I., Brandt, W. N., et al. 2006, *AJ*, **131**, 2826
- Tem, P., Brighenti, F., & Mathews, W. G. 2009, *ApJ*, **695**, 1
- Tonry, J. L., Dressler, A., Blakeslee, J. P., et al. 2001, *ApJ*, **546**, 681
- Trager, S. C., Worthey, G., Faber, S. M., Burstein, D., & Gonzalez, J. J. 1998, *ApJS*, **116**, 1
- Verbunt, F. 1987, *ApJL*, **312**, L23
- Voss, R., & Gilfanov, M. 2007, *MNRAS*, **380**, 1685
- Voss, R., Gilfanov, M., Sivakoff, G. R., et al. 2009, *ApJ*, **701**, 471
- Wong, K.-W., Irwin, J. A., Shcherbakov, R. V., et al. 2014, *ApJ*, **780**, 9
- Xue, Y. Q., Luo, B., Brandt, W. N., et al. 2011, *ApJS*, **195**, 1
- Zacharias, N., Urban, S. E., Zacharias, M. I., et al. 2000, *AJ*, **120**, 2131
- Zhang, Z., Gilfanov, M., & Bogdán, Á. 2012, *A&A*, **546**, A36
- Zhang, Z., Gilfanov, M., Voss, R., et al. 2011, *A&A*, **533**, A33